Bilayer tension-induced clustering of the UPR sensor IRE1

by

Md Zobayer Hossain

A thesis submitted in partial fulfillment of the requirements for the degree of

Master of Science

Department of Mechanical Engineering
University of Alberta

Abstract

The endoplasmic reticulum serves as a center for protein quality control, where chaperones and foldases facilitate protein folding. IRE1 is a transmembrane protein that transduces proteotoxic stress signals by forming clusters and activating the unfolded protein response (UPR). Recent research indicates that membrane thickness variation due to variations in membrane composition drives IRE1 cluster formation, activating the UPR even without proteotoxic stress. Based on the stability of the IRE1 dimer, we demonstrate a direct relationship between bilayer tension and UPR activation. The stability of the IRE1 dimer in a (50%DOPC-50%POPC) membrane at different applied bilayer tensions was analyzed via molecular dynamics simulations. For both tensed and compressed ER membranes, the potential of mean force for IRE1 dimerization predicts a higher concentration of IRE1 dimers. This study establishes a direct biophysical relationship between bilayer tension and UPR activation, demonstrating that IRE1 is a mechanosensitive membrane protein.

Preface

This thesis is an original work by Md Zobayer Hossain. Major parts of this thesis have been submitted for publication as Hossain, Md Zobayer & Stroberg, Wylie "Bilayer Tension induced clustering of UPR sensor IRE1", (submitted to BBA biomembrane). Md Zobayer Hossain was responsible for the theoretical developments, data analysis as well as the manuscript writing. Dr. Wylie Stroberg was the supervisory author and was involved with concept formations and manuscript revisions.

Acknowledgements

My sincere gratitude extends to Dr. Wylie Stroberg, my supervisor, without whom this thesis would never have been possible. His guidance and inspiration have motivated me to overcome the challenges efficiently. I sincerely thank my examining committee : Dr. Tian Tang, Dr. Maral Aminpour, and Dr. Benjamin Cheung for their invaluable time and effort in reviewing my thesis. I thank my parents and family for their support and love which keep me persistent and motivated. I also want to thank my friends and group members for their valuable suggestions and cooperation. I also want to thank the Digital research alliance of Canada for providing me with all the computational resources.

Table of Contents

List of Figures

List of Symbols

Constants

π	Ratio of circumference of circle to its diameter.	3.14
k_{B}	Boltzman constant.	$1.38064910 - 23\, m^2 kg s^{-2} K^{-1}$

Latin

$[A]$	Concentration of monomer
$[AA]$	Concentration of dimer
a	Unperturbed membrane thickness
a_{T0}	Unperturbed membrane thickness at bilayer tension zero
d_{ij}	distance between two coarse-grained bead of monomer A and j of monomer B
D_{p}	An index to quantify energetic cost of inserting protein in membrane
d_{rms}	1d reaction co-ordinate used in Replica exchange umbrella sampling.
d_c	Critical distance
E_{p}	Energy required for protein insertion in tensed membrane
$h(x, y)$	Membrane thickness at co-ordinate (x,y)
K_{d}	Dissociation constant
k_{t}^0	Thickness modulus of membrane at bilayer tension zero
N	Number of particles
n	number of particles in calculation of d_{rms}

P Pressure

P_z Pressure in the direction of membrane-normal

R Radius of the lipid area

T Temparature

u membrane deformation

y Time fraction of IRE1 dimer

Greek

β $1/k_{\mathrm{B}}T$

γ Bilayer tension

σ Area of lipid encompassing IRE1

Abbreviations

ATF6 Activating transcription factor 6.

BiP Binding immunoglobulin protein.

DOPC 1,2-Dioleoyl-sn-glycero-3-phosphocholine.

ER Endoplasmic reticulum.

ERAD Endoplasmic reticulum-associated degradation.

HAC1 homologous to ATF/CREB1.

IRE1 Inositol requiring enzyme1.

mRNA Messenger RNA.

PC Phosphatidylcholine.

PE phosphatidylethanolamine.

PERK Double stranded RNA-activated protein Kinase.

PMF Potential of mean force.

PO4 Coarse-grained phosphate ion.

POPC Palmitoyl-oleoyl-phosphatidylcholine.

REUS Replica exchange umbrella sampling.

RIDD Regulated IRE1 dependent decay.

RMSE Root mean square error.

RNA Ribonucleic acid.

rRNA Ribosomal RNA.

TIP3P Transferable Intermolecular Potential with Three Points.

tRNA Transfer RNA.

UPR Unfolded protein response.

VMD Visual molecular dynamics.

XBP1 X-box binding protein 1.

Chapter 1

Introduction

1.1 Motivation

The endoplasmic reticulum (ER) carries out a diverse range of functions including protein folding, synthesis and transport, lipid metabolic regulation, and calcium storage [Westrate et al., 2015, Clapham, 2007, Hebert et al., 2005, Fagone and Jackowski, 2009, Braakman and Hebert, 2013, Reid and Nicchitta, 2015, Rapoport, 2007]. Furthermore, the ER is a crucial center for protein quality control, where chaperones and foldases facilitate protein folding. However, when the concentration of molecular chaperones cannot meet the folding demands of nascent proteins in the ER, proteins often fail to fold correctly, accumulating misfolded or unfolded proteins in the ER lumen, which induces proteotoxic stress. To restore proteostasis in the ER and reduce proteotoxic stress, a broad range of responses collectively known as the unfolded protein response (UPR) is activated [Ron and Walter, 2007]. The UPR has three primary functions: suspension of protein translation, degradation of the misfolded protein, and increased folding capacity through the upregulation of genes encoding molecular chaperones. However, if the UPR fails to restore balance, apoptotic signals are initiated, leading to cell death [Szegezdi et al., 2006, Hetz, 2012]. The activation of the UPR and proteotoxic stress have been associated with various diseases, including neurodegenerative diseases [Hetz and Saxena, 2017], type 2 diabetes [Decio L and Miriam, 2010, Allen and David, 2010], obesity [Gökhan S, 2010], and cancer [Xuemei

et al., 2011].

Three transmembrane proteins located in the ER membrane are responsible for transducing signals of ER stress. These transducers, namely IRE1 (inositol requiring enzyme 1), PERK (double-stranded RNA-activated protein kinase [PKR]-like ER kinase), and ATF6 (Activating Transcription Factor 6), activate distinct UPR pathways to regulate proteostasis [Gardner et al., 2013]. In the case of IRE1, unfolded and misfolded proteins in the ER lumen facilitate the clustering of IRE1 by sequestering the chaperone BiP and stabilizing IRE1 oligomers [Calfon et al., 2002]. Clustered IRE1 produces transcription factors by splicing HAC1/XBP1 mRNA, which controls the expression of UPR target genes [Yoshida et al., 2001, Cox and Peter, 1996]. The IRE1 branch of the UPR regulates the load of protein folding by increasing the expression of ER chaperones and decreasing the translation of mRNA localized to the ER membrane through Regulated IRE1-Dependent Decay (RIDD).

Recently, even in the absence of proteotoxic stress, membrane aberancies have recently been shown to induce IRE1 clustering and UPR activation[Halbleib et al., 2017]. It was observed that changes in lipid composition of the ER membrane altered the membrane thickness and promoted IRE1 clustering. In the absence of proteotoxic stress, membrane thickness-mediated IRE1 clustering demonstrates a mechanism for activating the UPR. In this way, IRE1 shares a common regulatory mechanism with several other membrane proteins whose functions are dependent on the thickness of the lipid bilayer. For instance, MscL gating [Perozo et al., 2002], gramicidin signaling[Elliott et al., 1983], and the pseudoequilibrium of Rhodospin[Brown, 1994] are regulated by membrane thickness-mediated interactions.

The difference between the hydrophobic section of the transmembrane domain of membrane proteins and the thickness of the bilayer is known as hydrophobic mismatch [Mouritsen and Bloom, 1984, Sperotto and Mouritsen, 1988, Sperotto et al., 1989, Killian and Nyholm, 2006]. Hydrophobic mismatch results in local variations of membrane thickness around transmembrane proteins [Schmidt et al., 2008]. Al-

tered membrane thickness due to lipid compositional changes can therefore change the hydrophobic mismatch of embedded proteins, leading to structural reorganization or altered affinities for binding partners. In the case of IRE1, an elliptical depression forms around the protein due to an amphipathic portion that is constrained to sit at the interface between ER membrane and lumen. These depressions create a favorable environment for clustering since the clustersing allows the depressed regions around monomers to overlap, decreasing the free energy of the membrane-protein system. Through this clustering, the UPR is activated in the abesnce of proteotoxic stress [Halbleib et al., 2017].

Similar to compositional changes, direct application of bilayer tension alters membrane thickness [Rawicz et al., 2000, Muddana et al., 2011, Klauda et al., 2010, Reddy et al., 2012]. Membrane tension is linked to several cell functions like endocytosis and exocytosis [Pontes et al., 2017]. In the ER, membrane tension influences lipid budding [Ben M'barek et al., 2017]. Cytoskeletal forces and lipid composition also contribute to tension in the cell membrane [Pontes et al., 2017]. Similarly, tension in ER will also be affected by cytoskeletal forces and lipid composition. Tension applied to the membrane surface changes the area per lipid and membrane thickness, which impacts the overall packing density of lipids and proteins in the ER. As a result, ER tension will reorder the protein-lipid arrangement. Since bilayer tension is instrumental to changes in membrane thickness and packing density, I hypothesize that it also modulates the stability of IRE1 clusters.

1.2 Thesis objectives

This study determines the influence of membrane tension on IRE1 clustering through coarse-grained molecular dynamics simulations. In addition to responding to protein concentration in the ER lumen and lipid composition in the ER membrane, these simulations demonstrate that IRE1 is also sensitive to mechanical perturbations of the ER membrane. The free energy difference between the IRE1 dimer and monomer

states is used as an index for assessing the stability of IRE1 dimer under various tensions.

1.3 Thesis outline

In Chapter 2, I provide the necessary context to understand the role of IRE1 in activating the UPR and maintaining homeostasis in the ER. In Chapter3, I describe the molecular dynamics simulation techniques used to capture the behavior of the transmembrane portion of IRE1 in the ER. In Chapter 4, I describe how membrane tension affects the stability of IRE1 dimers. In Chapter 5, I interpret the free energy landscape of IRE1 dimerization in the tensed ER to build a biophysical connection between tension and the UPR. Finally, in Chapter 6, I conclude our study.

Chapter 2

Background

2.1 Endoplasmic reticulum (ER)

2.1.1 Structure of ER

The endoplasmic reticulum (ER) is a vast cell organelle with diverse cellular functions like protein synthesis, folding and transport, calcium storage, lipid metabolism, etc [Westrate et al., 2015, Clapham, 2007, Hebert et al., 2005, Fagone and Jackowski, 2009, Braakman and Hebert, 2013, Reid and Nicchitta, 2015, Rapoport, 2007]. ER is composed of phospholipids, cholesterol, and various proteins. ER is shaped into a continuous membrane network of tubules and sheets [Voeltz and Prinz, 2007, Hu et al., 2011, Shibata et al., 2006, English et al., 2009, Friedman and Voeltz, 2011, English and Voeltz, 2013]. Phospholipids form the main structure of ER. The polar phosphate group of the lipid is hydrophilic, whereas the fatty acid part of the lipid molecule is hydrophobic. Phospholipid is an amphiphilic molecule with both hydrophobic and hydrophilic portions. The hydrophobic phosphate group is termed the lipid head, and the hydrophilic fatty acid portion is called the lipid tails. When lipid molecules come into contact with an aqueous environment, lipid tails minimize their exposure to water by forming a bilayer. A schematic of the lipid bilayer is shown in Fig. 2.1b. ER also houses several proteins. ER can be classified into two classes based on ribosomes on its outer surface, (i) rough endoplasmic reticulum- has ribosomes on its surface (ii) smooth endoplasmic reticulum- has no ribosomes [Alberts et al., 2017].

A schematic of an animal cell with both types of ER is shown in Fig. 2.1a.

2.1.2 ER functions

The rough endoplasmic reticulum takes part in several cellular functions like protein synthesis, sorting, and degradation. Ribosomes in the rough endoplasmic reticulum combine the amino acids to synthesize protein. Newly manufactured protein enters ER lumen and undergoes post-translational modifications like folding, glycosylation, and disulfide bond formation, which are necessary for their proper function [Alberts et al., 2017]. Rough ER also sort newly folded protein via a dynamic cellular program called "protein sorting" to transport proteins to cellular destination. Unfolded protein in ER lumen is sensed by ribosomes and sent to degradation to maintain protein quality in ER lumen. The smooth endoplasmic reticulum also performs several cellular functions like lipid metabolism, calcium ion storage, carbohydrate metabolism, and detoxification. In lipid metabolism, ER breakdowns and store the fat and uses the stored fat to synthesize functional lipids [Krahmer et al., 2013]. The smooth endoplasmic reticulum of muscle and nerve cells stores calcium ions; calcium balance is crucial for several cellular functions like muscle contraction, neurotransmitter release, and cellular signaling [Clapham, 2007]. Smooth ER can metabolize and regulate carbohydrates [Stigliano et al., 2011]. Through biotransformation, the smooth endoplasmic reticulum converts the foreign particles of the body into more water-soluble to detoxify.

2.2 Protein synthesis

Proteins are synthesized via a process called "protein synthesis." Protein synthesis comprises two processes: (i) transcription and (ii) translation [Alberts et al., 2017]. To perform translation and transcription, three types of RNA- a single-stranded molecule is produced via an enzyme called RNA polymerase. These are (i) messenger RNA (mRNA), (ii) ribosomal RNA (rRNA), and (iii)transfer RNA (tRNA). RNA is pro-

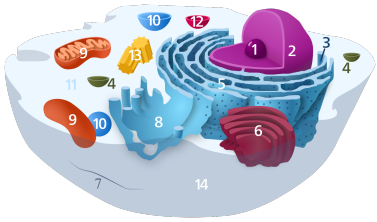

(a) Various components of animal cell: 1.Nucleolus, 2. Nucleus, 3. Ribosome (dots as part of 5), 4. Vesicle, 5.Rough endoplasmic reticulum, 6. Golgi apparatus, 7. Cytoskeleton, 8. Smooth endoplasmic reticulum, 9. Mitochondrion, 10. Vacuole, 11. Cytosol, 12. Lysosome, 13. Centrosome, 14. Cell membrane. Between the smooth and rough endoplasmic reticulum is the presence of ribosomes on rough endoplasmic reticulum. Image is reprinted from the work of Kelvin song under public domain.

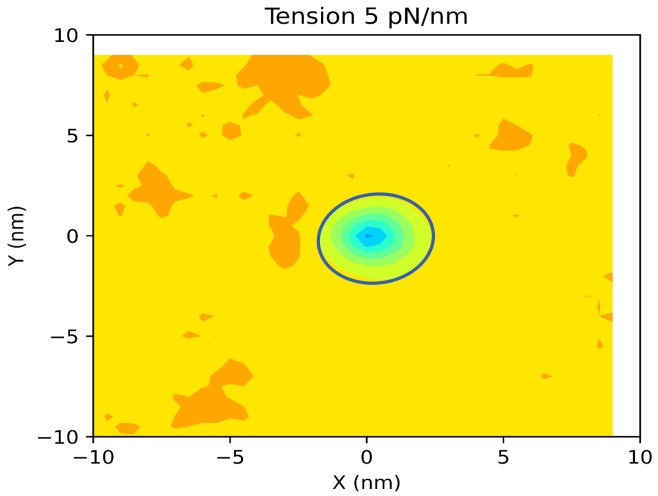

(b) A schematic view of lipid bilayer with IRE1, a transmembrane protein. Hydrophilic lipid tails(hydrocarbon chain) forms a bilayer to minimize it's exposure to water molecules. Distance between the phosphate group of the each leaflet is the membrane thickness IRE1 works as sensory protein for Unfolded protein response. IRE1 has RNase and KiNase on the cytosolic side.

Figure 2.1: Schematic view of animal cell and lipid bilayer.

duced in the nucleus in eukaryotes, whereas RNA is produced in the cytoplasm in the case of prokaryotes. In transcription, code for the protein sequence is copied from the gene into the messenger RNA (mRNA). mRNA is further modified to prevent degradation and facilitate export to the protein synthesis site. Protein synthesis site, ribosomes are formed by rRNA molecules. During translation, tRNA molecules transport the amino acids to ribosomes, and with the help of genetic code copied into mRNA, ribosomes assemble the amino acids to synthesize a protein. Newly synthesized proteins enter the ER lumen. Molecular chaperones work as folding machinery for newly formed proteins. Molecular chaperons fold newly synthesized protein into a three dimensional structure. This three dimensional structure is very essential for proper functioning of these proteins. These folded proteins can stay in the ER or export to the golgi apparatus to reach their destination. The destination signal is added during protein sorting, where ER retention signal instructs the protein to stay in ER, and ER export signal instructs it to export to other cellular compartments. A schematic of protein synthesis is shown in Fig. 2.2

2.3 Unfolded protein response(UPR)

Molecular chaperones fold newly synthesized protein in ER lumen [Hartl, 1996]. However, the need for more molecular chaperones compared to the folding demand creates a situation where all proteins can not be folded. This misfolded/unfolded protein accumulates in the ER and creates proteotoxic stress on the ER. To eliminate this proteotoxic stress and restore the protein quality in ER lumen, a homeostatic program called Unfolded Protein Response (UPR) is initiated [Ron and Walter, 2007, Hetz, 2012]. UPR tries to maintain proteostasis through three primary functions (i) increase folding capacity of ER- by upregulation of genes encoding molecular chaperones, (ii) suspension of protein translation- which reduces the folding load compared to available molecular chaperons, and (iii) protein degradation in a programmed so that protein folding load is reduced [Walter and Ron, 2011]. These functions restore

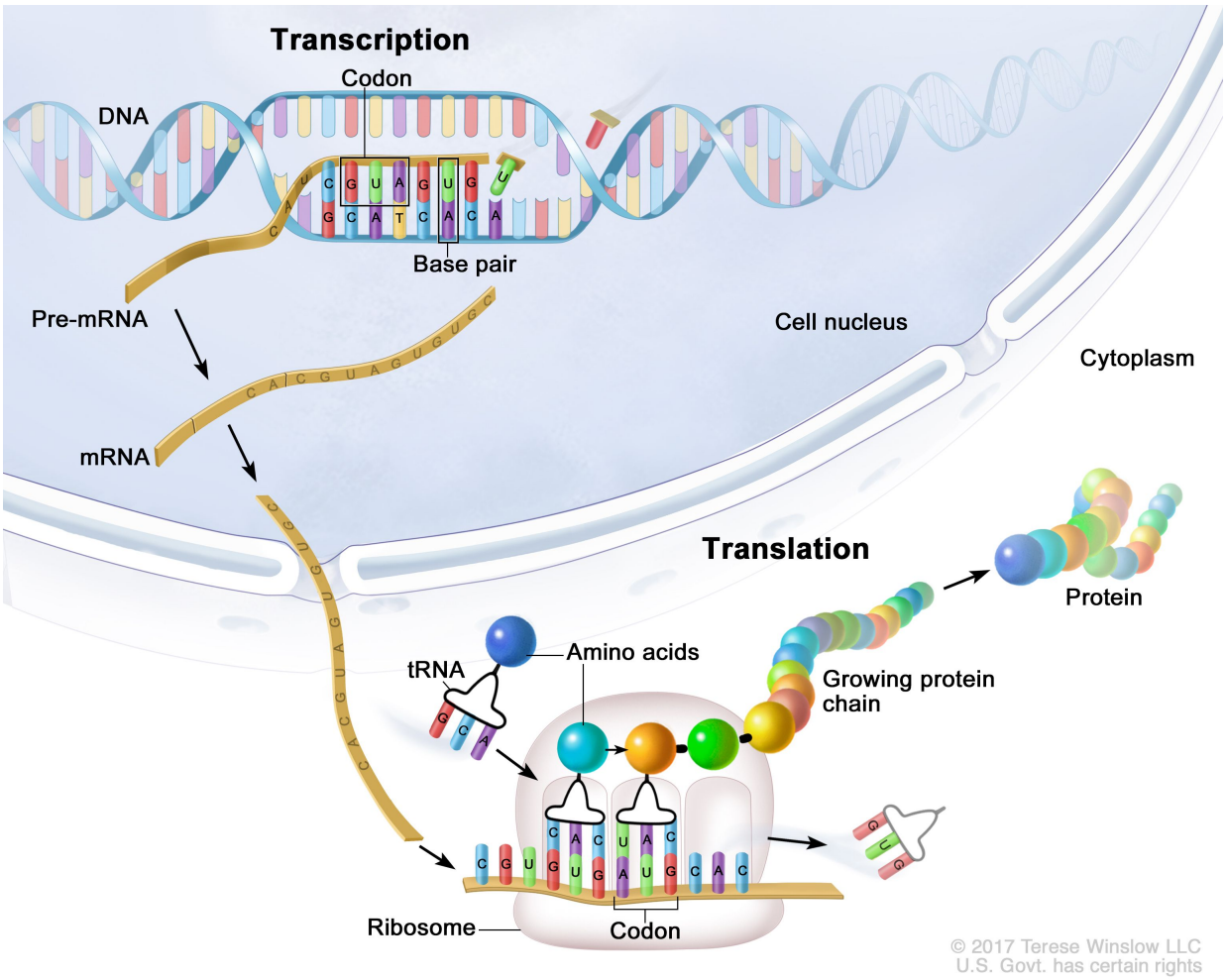

Figure 2.2: Protein synthesis: During transcription, genetic code for protein sequence is copied into mRNA from DNA in cell nucleus. After translocating the mRNA into ribosome of rough endoplasmic reticulum, ribosomes synthesize protein by assembling the amino acids brought by tRNA according to the code of mRNA. Newly synthesized protein enters in ER lumen where it goes under several post translational modification. Image is reprinted with permission of Terese Winslow LLC. Credit: For the National Cancer Institute © 2017 Terese Winslow LLC, U.S. Govt. has certain rights.

a balance between molecular chaperons and folding demand. If these functions fail to restore proteostasis, UPR initiates cell death via a cell suicidal program called apoptosis [Lin et al., 2007]. Hence, UPR influences the cell's fate.

2.4 IRE1 activated UPR

Three ER stress sensors sense the unfolded/misfolded protein in ER and activate UPR. These are IRE1 (inositol requiring enzyme 1), PERK (double-stranded RNA-activated protein kinase [PKR]-like ER kinase), and ATF6 (Activating Transcription Factor 6) [Gardner et al., 2013, Walter and Ron, 2011]. A figure illustrating the activation pathway of UPR via IRE1 is shown in Fig. 2.3. IRE1 is a single-pass transmembrane protein with a kinase and RNase domain on its cytosolic side. In the presence of unfolded protein in ER lumen, BiP, a chaperon protein, isolates from the IRE1 monomer and attach to the unfolded protein [Bertolotti et al., 2000]. IRE1 monomers without the BiP, form the IRE1 cluster [Korennykh et al., 2008]. Clustered IRE1 activates cytosolic kinase and RNase domain [Morl et al., 1993, Cox et al., 1993, Sidrauski and Walter, 1997]. Activated RNase domain spliced mRNA of HAC1 in S. cerevisiae and XBP1 in vertebraes. The spliced form of HAC1/XBP1 travels to the nucleus and works as a transcription factor to activate UPR genes. IRE1-activated UPR genes restore the proteostasis in ER by reducing the protein translation or degrading the misfolded/unfolded protein via a cellular program, "ERAD" [Ron and Walter, 2007]. ERAD breaks down the unfolded/misfolded proteins in ER into smaller peptides and reduces the proteotoxic stress on ER [Vembar and Brodsky, 2008, Smith et al., 2011]. So, the IRE1 clustered are formed upon presence of unfolded protein and activate UPR. BiP attachment to IRE1 works as regulator for duration of IRE1 cluster form.

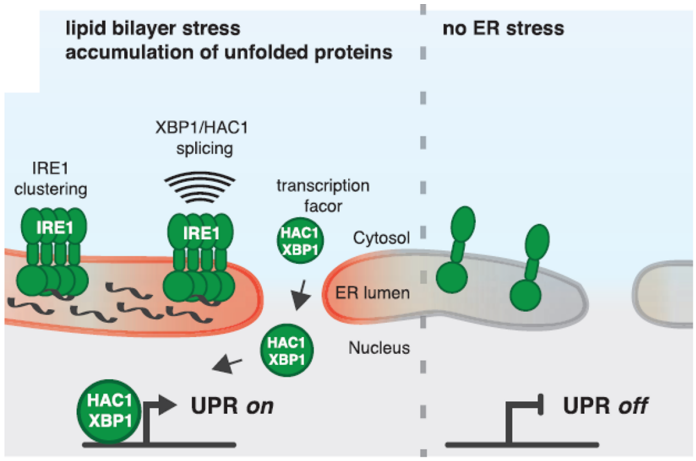

Figure 2.3: UPR activation by IRE1, a sensory transmembrane protein. Presence of undfolded protein favors IRE1 clustering. Lipid bilayer stress also influence IRE1 clustering. IRE1 oligomer splices the XBP1/HAC1, spliced form of sXBP1/sHAC1 works as transciption factor. sXBP1/sHAC1 activates the UPR genes which tries to restore ER homeostasis by reducing the protein load in ER lumen. Upon elimination of ER stress, IRE1 oligomers breaks into monomers which results into no transcription factor for activating UPR. Hence, UPR is deactivated. Image is reprinted from "Covino, R., Hummer, G., & Ernst, R. (2018). Integrated functions of membrane property sensors and a hidden side of the unfolded protein response. Molecular cell, 71(3), 458–467" with permission from Elsevier. [Covino et al., 2018].

2.5 Lipid bilayer stress activated UPR

Studies have shown alterations in lipid bilayer environments like a perturbed ratio of phosphatidylethanolamine (PE) to phosphatidyl-choline (PC) [Thibault et al., 2012], increased lipid saturation [Surma et al., 2013], increased sterol levels [Pineau et al., 2009], and inositol depletion required for the synthesis of phosphatidylinositol (PI) and yeast sphingolipids [Promlek et al., 2011] also influenced the IRE1 clustering. So, these membrane aberrancies acted as an additional activator of UPR. These membrane aberrancies are collectively termed lipid bilayer stress [Surma et al., 2013]. The amphipathic helix and transmembrane domain of IRE1 make it sensitive to lipid bilayer stress. The amphipathic helix of IRE1 lies at the membrane surface to accommodate polar and non-polar faces [Halbleib et al., 2017]. The hydrophobic mismatch is the difference between the hydrophobic section of the transmembrane domain of membrane proteins and the thickness of the bilayer [Killian, 1998]. Due to hydrophobic mismatch and IRE1's amphipathic helix, IRE1 monomers compress the lipid bilayer at the insertion point. Any perturbation in ER increases the energetic cost of compressing the membrane around the protein inclusions [Halbleib et al., 2017]. Membrane compression is quantitatively expressed as membrane deformation. Membrane deformation is the difference between the membrane thickness around the protein inclusion and the unperturbed membrane thickness. IRE1 creates a more pronounced deformation in thicker membranes compared to thinner membranes [Halbleib et al., 2017]. This increased membrane deformation makes it challenging for the IRE1 dimer to dissociate in a thicker membrane than a thinner one. So, IRE1 dimers are more stable in thicker membranes, and IRE1 oligomers in thicker membranes activate UPR [Halbleib et al., 2017].

2.6 Hypothesis of tension mediated UPR activation

Ostomic pressure difference, cytoskeletal forces and, lipid composition contribute to the tension in the membrane [Pontes et al., 2017, jea]. Membrane tension is defined as the mechanical force applied to induce tensile or compressive stress at membrane surface. Considering infinitesimal membrane surface, membrane tension is the force required to increase the membrane surface of this infinitesimal body per unit length 2.4 . Through expansion/compression of membrane surface, membrane tension impacts the ER's physical properties, like membrane thickness, area per lipid, and lipid ordering [Rawicz et al., 2000, Muddana et al., 2011, Klauda et al., 2010, Reddy et al., 2012]. Membrane tension has been seen to impact cell functions like endocytosis and exocytosis [Pontes et al., 2017]. In ER, membrane tension influences functions like lipid budding [Ben M'barek et al., 2017]. Regulating membrane tension will modulate membrane thickness and area per lipid. In altered tensed state, lipid-protein arrangement will rearrange the lipid molecules around the protein. Rearranged lipid-protein packing will influence the energetic cost of the depressing membrane around the IRE1. The previous section showed that several perturbation in ER environment impacts the IRE1 clustering phenomena 2.5. So, I hypothesize that properties of ER under tension will affect the IRE1 clusters and thus modulate UPR.

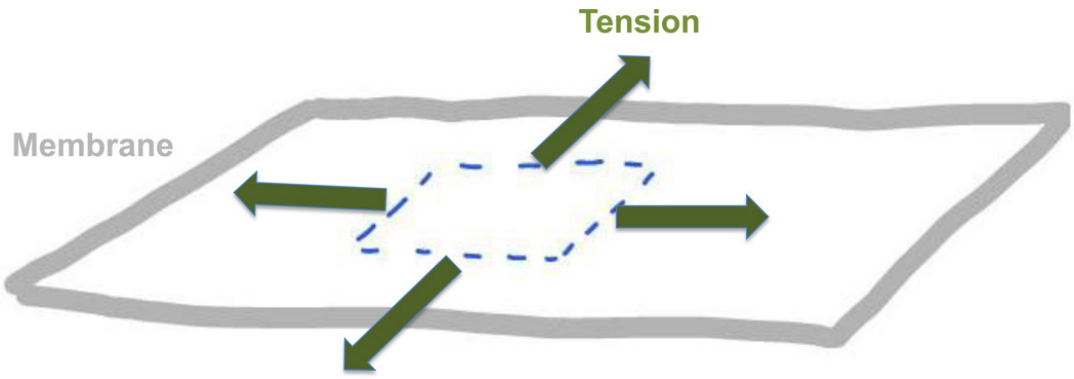

Figure 2.4: Tension in a membrane. Tension, γ is applied along the imaginary boundary of infinitesimal membrane surface. This image is reprinted from "Kozlov, M. M., & Chernomordik, L. V. (2015). Membrane tension and membrane fusion. Current opinion in structural biology, 33, 61–67." with permission from Elsevier [Kozlov and Chernomordik, 2015]

Chapter 3

Methods

In the following chapter, simulation techniques and parameters used to calculate free energy landscapes of IRE1 dimerization in the ER are discussed in detail. First, I model the atomic structure of the transmembrane portion of IRE1, IRE1$^{516\text{-}571}$. After validation of the atomistic structure, I built a coarse-grained structure of IRE1$^{516\text{-}571}$ from the atomistic model. Then, to estimate the free energy difference I have used replica exchange-umbrella sampling.

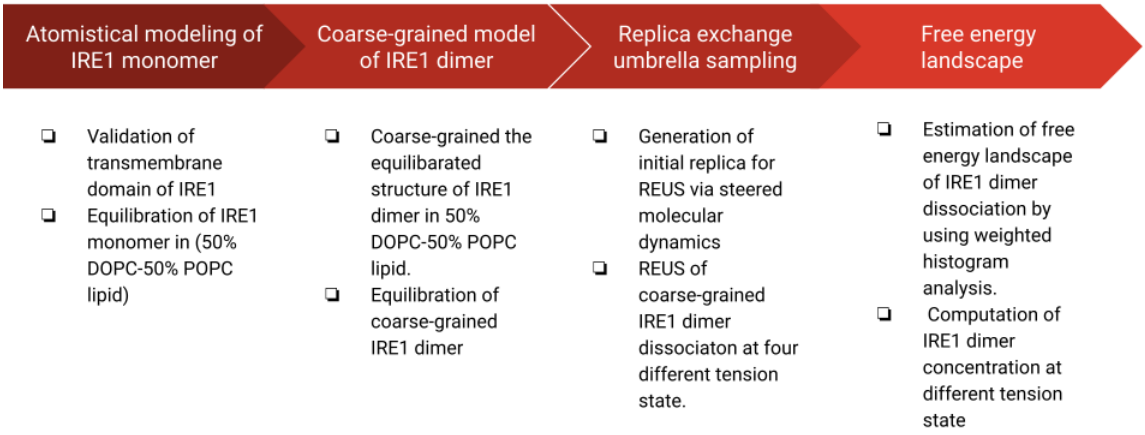

Figure 3.1: Workflow of the study.

3.1 Atomistic modeling of IRE1 sensor peptide

The transmembrane portion of $IRE1^{516\text{-}571}$ was adopted from the study of Halbleib et al. where they have shown that the transmembrane domain is sensitive to lipid bilayer stress, leading to UPR activation. [Halbleib et al., 2017]. The 56 amino acid long sequence "516-SRELD EKNQNSLLLK FGSLVYRIIE TGVFLLLFLI FCAILQRFKI LPPLYVLLSK I-571" consists of a transmembrane helix and an amphipathic helix [Halbleib et al., 2017]. The IRE1 peptide was built from the sequence via the molefacture plugin of Visual Molecular Dynamics (VMD) [Humphrey et al., 1996]. $IRE1^{516\text{-}571}$ was inserted into an equilibrated lipid bilayer of (50%-50%) DOPC-POPC via the membrane builder of the CHARMM-GUI [Jo et al., 2008, Brooks et al., 2009, Lee et al., 2016, Jo et al., 2009, Lee et al., 2019]. This membrane protein complex consists of a single $IRE1^{516\text{-}571}$ monomer, 310 DOPC(1,2-Dioleoyl-sn-glycero-3-phosphocholine), 310 POPC (1-Palmitoyl-2-oleoyl-sn-glycero-3-phosphocholine) and 33702 TIP3P water molecules. For ionic balance, 91 sodium and 97 chloride ions were also inserted. The simulation box dimensions are 14.8 nm x 14.8 nm x 9.27 nm. The CHARMM36 force field was used for all simulations. After energy minimization, the model structure was first equilibrated while constraining the positions of lipid heads and protein. Another constraint was used to keep the water out of the hydrophobic core of the structure. After equilibration of 0.375 ns with time step 1 fs, the timestep was increased to 2 fs, and the system was equilibrated for an additional 0.5 ns. Next, a production run of 200 ns was carried out without constraints. All the simulations were run in the NPT ensemble by applying a Langevin thermostat at 303.15 K and Nose Hoover-Langevin piston barostat at 1 bar.

3.2 Coarse-grained IRE1 dimer

Atomistic simulation captures the fine atomic interactions and provide more details about the system. But large atom numbers (in my case, $\approx$ 180000) and time step

of 2 fs makes atomistic simulations too expensive to achieve adequate sampling for replica-exchange umbrella sampling simulations. By coarse-graining the atomistic model, the degrees of freedom of the system can be reduced to make the simulation less expensive. Also, coarse-graining groups of atoms into a single bead allows the use of a larger time step (typically 20 fs). Reduced atom numbers and larger time steps make coarse-grained molecular dynamics simulation computationally significantly less expensive than the atomistic simulation. As some of the details are lost while coarse-graining, coarse-grained simulation can not provide the same resolution as atomistic simulation but can provide a good approximation of long timescale phenomena. Hence, I opted for coarse-grained simulation for this study. The equilibrated structure of $IRE1^{516\text{-}571}$ was extracted from the atomistic model. Two identical replicas of $IRE1^{516\text{-}571}$ were placed such that the distance between carbon-β atoms of F544 residues of each monomer was 0.7 nm using VMD [Humphrey et al., 1996]. Monomers were oriented in an X-like configuration that has been shown to be the orientation of assembled full length IRE1 [Väth et al., 2021]. The dimer was coarse-grained using CHARMM GUI's MARTINI Maker to produce a coarse-grained membrane protein complex [Hsu et al., 2017]. The coarse-grained model consists of 2 $IRE1^{516\text{-}571}$ monomers, 574 DOPC and 574 POPC, and 22775 MARTINI water molecules. 270 negative ions and 270 positive ions were inserted into the system to make the system neutral. The dimension of the model is 20 nm x 20 nm x 10.15 nm. The MARTINI force field 2.0 was used for all interactions [Marrink et al., 2007]. After energy minimization, a short equilibration run was performed with the positions of lipid heads and proteins constrained. Next, the unconstrained system was equilibrated for 200 ns. All simulations were run in the NPT ensemble by applying a Langevin thermostat and Nose-Hoover barostat at 303.15 K and 1 bar.

3.3 Molecular dynamics and analysis softaware

All molecular dynamics simulations were performed using the molecular dynamics simulation package, NAMD [Phillips et al., 2020]. VMD was used to create all visual representations [Humphrey et al., 1996]. Membrane thickness of the trajectories were calculated via MEMBPLUGIN of VMD [Guixà-González et al., 2014]. The membrane thickness was described as the distance between the coarse-grained lipid heads (PO4 bead) of the top and bottom leaflets of the membrane. The colvar module was used to define the reaction coordinate and run steered molecular dynamics in NAMD [Fiorin et al., 2013]. Python 3.0 was used for data analysis and visualization. WHAM, an implementation of the weighted histogram analysis method, was used to calculate free energies from umbrella sampling simulations [Grossfield].

3.4 Replica-exchange umbrella sampling

Free energy landscapes are estimated with reference to a reaction co-ordinate, which is a low-dimensional representation of the process of interest. The reaction co-ordinate is based on the atomic co-ordinates of the system and seeks to capture the relevant features of a process by mapping the high-dimensional phase space of the system to one (or a few) dimensions. The high dimensional movement of biomolecules makes estimating free energy computationally expensive. However, the low-dimensional representation of the system in the reaction coordinate (also called the collective variable) allows the free energy of a process such as dimerization to be estimated more efficiently. To explore various conformation, biomolecules have to overcome a energy barriers that separate local minima 3.2a. In Fig. 3.2a a schematic free energy plot as a function of a collective variable that separates two energy wells is shown. Transitions from state B to state A requires overcoming a energy barrier at state C. Since the probability of spontaneously observing the molecular transition from state B to state A is very low, sampling the free energy landscape is generally computationally expen-

sive. To overcome this problem, several enhanced algorithms are used to sample the various configuration of membrane-protein and to accelerate the convergence of free energy landscape. The sampling techniques can be classified into two categories, (ii) collective variable based (CV) and (ii) CV free techniques. Widely used CV based samplings are Umbrella sampling [Torrie and Valleau, 1977], metadynamics [Laio and Parrinello, 2002], steered molecular dynamics [Lu and Schulten, 1999], adaptive biasing force [Darve et al., 2008], conformational flooding [Grubmüller, 1995], string method [E et al., 2002], and temperature accelerated molecular dynamics [Maragliano and Vanden-Eijnden, 2006]. Convergence of these sampling techniques depend on the efficient definition of collective variable. Sometimes, it becomes very complex to define a proper CV because of the complexity of biological systems. CV free techniques like replica exchange [Sugita and Okamoto, 1999], and accelerated molecular dynamics [Hamelberg et al., 2004] doesn't require prior knowledge to define collective variable. A combination of both CV based and CV free techniques like replica-exchange umbrella sampling is widely used for quicker convergence of free energy landscape. In umbrella sampling, the reaction co-ordinates are discretized into several bins. In each of the bins, a harmonic potential is applied to bias certain configurations that would otherwise be observed only rarely. The biased sampling allows the entire free energy landscape across a reaction co-ordinate to be sampled with much less computational expense. The harmonic potential applied to the system in window i is

$$V_{\mathrm{i}}(c_{\mathrm{i}}) = \frac{k}{2}(c_{\mathrm{i}} - c_0)^2, \tag{3.1}$$

where c_{i} and c_0 are reaction coordinate of the i^{th} window and reference reaction coordinate value at the i^{th} window.In, each window, an independent copy of system is placed with different specified initial condition like reference reaction coordinate system. These identical copies of the system is known as replica. Harmonic potential applied tries to pull the replicas to it's reference reaction coordinate of the corresponding window. To further enhance sampling, replicas in various windows are attempted

to exchange at specified simulation intervals. Exchange between the replicas of the windows are based on the Metropolis criterion. The probability of exchanging replicas between window m and n is given by

$$P(m \rightarrow n) = \min \left[1, e^{-\frac{(E_{\mathrm{m}} - E_{\mathrm{n}})}{k_{\mathrm{B}} \cdot T}} \right] \tag{3.2}$$

where E_{m} and E_{n} represents the potential energy of the replica at window m and n respectively. k_{B} and T represents the Boltzman constant and temperature respectively. If the exchange results in the decrease of potential energy, exchange is permitted. Otherwise the exchange is prohibited and an exchange is tried at the next interval. Exchanging replicas between windows ensures greater exploration of conformational space. The frequency of attempted exchanges is also an important parameter for enhanced sampling. Optimal exchange attempting frequency ensures an efficient sampling with efficient computational cost. Hence, umbrella sampling combined with replica exchange provides a more computationally efficient sampling method to estimate free energy landscapes than using umbrella sampling alone. Replica-exchange umbrella sampling (REUS) was implemented with the replica-exchange module of NAMD. The colvar module was used to specify the reaction coordinate and to record trajectory data. The root mean square of the inter-particle distance between backbone coarse-grained beads of IRE1 monomers, d_{rms}, was used as the reaction coordinate. Even though d_{rms} is a 1D reaction coordinate, it was chosen specifically to capture some rotational degree of freedom along with the center of mass separation. d_{rms} is defined as

$$d_{\mathrm{rms}} = \frac{\sqrt{\sum_{i,j=1}^{n,n} d_{ij}^2}}{n} \tag{3.3}$$

where d_{ij} is the distance between backbone bead i of monomer A and bead j of monomer B and n is the number of backbone beads considered in each of the monomers.

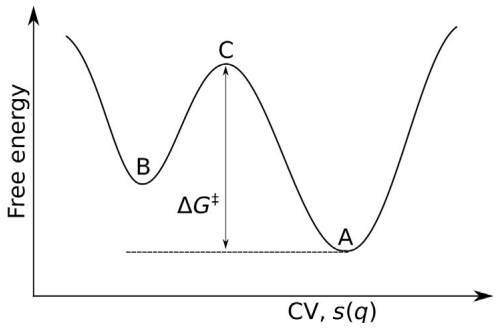

(a) Energy barrier between State A and State B. Transition from state B to state A must overcome an energy barrier at state C. Image is reprinted from "Liao, Q. (2020). Enhanced sampling and free energy calculations for protein simulations. in Computational Approaches for Understanding Dynamical Systems: Protein Folding and Assembly (pp. 177–213)." with permission from Elsevier [Liao, 2020].

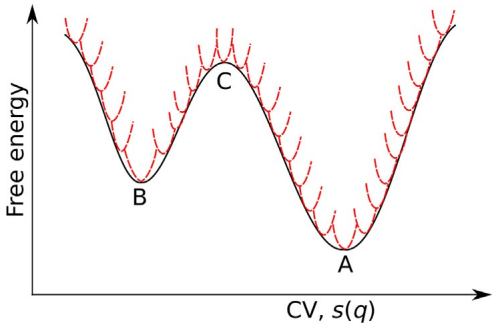

(b) Schematic of umbrella sampling scheme. Free energy is estimated against a collective variable, CV,s(q). Total CV space is divided into small windows. In each windows, simple harmonic potential (red dash line) was added to the system Hamiltonian. Image is reprinted from "Liao, Q. (2020). Enhanced sampling and free energy calculations for protein simulations. Computational approaches for understanding dynamical systems: protein folding and assembly (pp. 177–213)." with permission from Elsevier [Liao, 2020].

Figure 3.2: Schematic view of energy barrier and umbrella sampling.

From the simulation of IRE1$^{516\text{-}571}$ monomer in the ER, I have found three distinct portions of IRE1$^{516\text{-}571}$: IRE1$^{526\text{-}544}$ sits on top of the lipid surface on the lumenal side, IRE1$^{545\text{-}552}$ is fully inserted into the lipids, and IRE1$^{553\text{-}571}$ is situated close to the cytosolic side (Fig. 3.3). To capture the movement in a computationally efficient manner, the backbone beads of IRE1$^{544\text{-}552}$ were used in calculating d_{rms}. Replica-exchange umbrella sampling was implemented with 35 evenly spaced bins over a range of 0.5∼7 nm (0.2 nm/bin). Replicas for the various bins were prepared using SMD with a spring constant of 25 kcal/molÅ^2. In replica-exchange umbrella sampling, a harmonic restraint of 2.5 kcal/molÅ^2 was applied to sample the replicas in various bins. Convergence analysis of replica-exchange umbrella sampling simulations are added in the A.1.

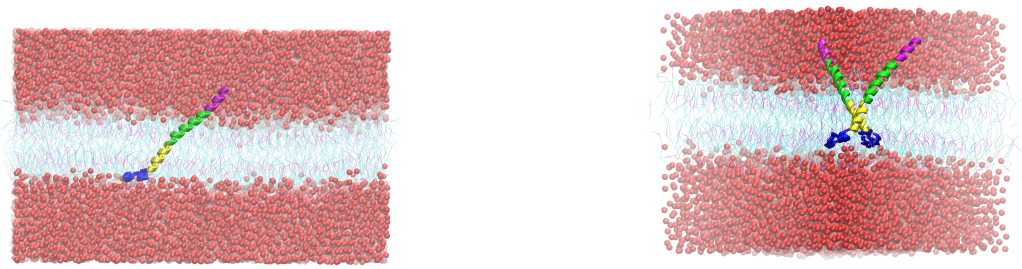

(a) IRE1$^{516\text{-}571}$ monomer. (b) IRE1$^{516\text{-}571}$ dimer.

Figure 3.3: Coarse-grained IRE1$^{516\text{-}571}$ in (50%-50%) DOPC-POPC membrane. The amphipathic portion of the IRE1, IRE1$^{526\text{-}544}$(green helix) lies at the interface between the membrane top surface and the ER lumen. The rest of IRE1$^{544\text{-}571}$(yellow and blue helix) sit inside the membrane. The purple helix is the IRE1$^{516\text{-}525}$ on the ER lumenal side. Water is represented by red beads. Lipids are represented as violet and cyan lines.

3.5 Weighted histogram analysis method

The weighted histogram analysis method (WHAM) is a computational method used to estimate free energy landscapes from trajectories of molecular dynamics simulation. WHAM analyzes the probability distribution of discrete states and estimates the free energy of the state. The probability distribution of each state can be calculated from

the histogram of conformations in a certain state. The free energy difference between state j and l is related to the transition probabilities from state j to l, P_{jl} and from l to j, P_{lj}, as

$$\Delta F_{\mathrm{jl}} = -k_B T \ln\left(\frac{P_{\mathrm{lj}}}{P_{\mathrm{jl}}}\right), \tag{3.4}$$

where k_B is the Boltzmann constant and T is the temperature.

To calculate P_{jl}, the probability distribution in each state is required. Since REUS applied a harmonic biasing potential V_{j} in each window for biased sampling, the probability distribution of window j, P_{j} from the simulation is biased. Biased probability distribution can be unbiased by

$$P^0_{\mathrm{ij}} = \frac{P_{\mathrm{ij}} e^{\beta V_{\mathrm{j}}}}{f_{\mathrm{ij}}}, \tag{3.5}$$

where P^0_{ij} is the unbiased probability distribution at window j from the i^{th} simulation and f_{ij} is a normalizing constant so that summation of P_{ij} over the whole conformation space is one: $\sum_i P_{ij} = 1$. An optimized estimate of P^0_{j} is given by following equation

$$P^0_{\mathrm{j}} = \frac{\sum_i^S n_{ij}}{\sum_i^S N_i f_i e^{-\beta V_{\mathrm{j}}}} \tag{3.6}$$

Where S is the total simulation, n_{ij} is the population in the window j of the i^{th} simulation, and N_i is the total number of samples in the i^{th} simulation. The unbiased probability distribution is also constrained by the normalizing condition

$$f_i^{-1} = \sum_{j=1}^{M} e^{-\beta V_{\mathrm{j}}} P^0_{ij}. \tag{3.7}$$

By solving equation 3.6 and 3.7 iteratively the optimal estimate of P^0_{j} can be found within a certain convergence limit. The unbiased probability distribution is then used to calculate the free energy landscape by equation3.4.

3.6 Bilayer tension implementation

The surface tension target feature of NAMD was used to regulate bilayer tension in the simulations. The tension, γ was applied along the membrane surface. The pressure normal to the membrane surface, P_z=1 atm. was applied via a Langevin piston. The free energy of IRE1$^{516\text{-}571}$ dimer dissociation was calculated at four different bilayer tensions, γ [15,5,0,-5] pN/nm in the $NP_z\gamma T$ ensemble. Bilayer tensions of positive values indicates tension while negative values indicate compression.

3.7 Dissociation constant of IRE1 dimerization

The dissociation constant of IRE1 dimerization was calculated via the following equation

$$K_d = \frac{(1-y)[A][A]}{y[AA]} \tag{3.8}$$

where $[A]$ is the concentration of IRE1 monomer, $[AA]$ is the concentration of IRE1 dimer, and y is the time fraction of IRE1 dimer state. Equation (3.8) was previously used to calculate K_d for GpA dimers from molecular dynamics simulation [Domański et al., 2017]. Equation (3.8) was derived based on the following equilibrium properties: (i) at equilibrium the time-average forward and backward rates of dimerization are equal; and (ii) the time-average of the chemical potential of the monomer and dimer at equilibrium are equal. In the dimer state, the concentration of the dimer is, $[AA] = 1/\sigma$ and in the monomer state, $[A] = 2/\sigma$, where σ represents the area of lipids enclosed by two monomers when they are a furthest apart in the simulation. In this case, $\sigma = \pi R^2/4$, where R is the distance between the two IRE1 monomers in the farthest bins of the umbrella sampling simulations. By putting these values into Equation (3.8), I obtain

$$K_d = \frac{\frac{(1-y)2^2}{\sigma^2}}{\frac{y}{\sigma}} = \frac{4(1-y)}{\sigma}. \tag{3.9}$$

The time fraction of the dimer was determined by the following equation

$$y = \frac{\int_0^{d_c} e^{-\beta F(d_{rms})}\, d(d_{rms})}{\int_0^{d_c} e^{-\beta F(d_{rms})}\, d(d_{rms})}, \tag{3.10}$$

where $\beta = \frac{1}{k_B T}$, k_B and T represent Boltzmann's constant and the absolute temperature, respectively. The critical distance, d_c, separates the region of the dimer state from the monomer state. It was shown previously shown that y is relatively insensitive to the choice of d_c [Domański et al., 2017]. As, the free energy landscape under tension is altered, the boundary separating the monomer and dimer regions is also changed. The boundary line d_c differentiating the dimer and monomer can be estimated from the free energy landscape. As the free energy landscapes were different under different tension, d_c values were also different for each tension cases.

Chapter 4

Results

The free energy landscapes of IRE1$^{516\text{-}571}$ dimerization under tension and compression estimated by replica-exchange umbrella sampling simulations are presented in this chapter. First, the effect of tension on the membrane was assessed. Next, I calculated the change in local membrane depression around an IRE1 monomer. Finally, I determine how the PMF for dimerization is altered by tension and compression. From these results, I estimate the percentage of IRE1$^{516\text{-}571}$ dimer at different IRE1 concentrations as a proxy of UPR activation.

4.1 Tension modulates ER bilayer shape

4.1.1 Bilayer tension decreases the membrane thickness while compression increases the membrane thickness

To determine the effect of membrane tension on bilayer thickness, tension was applied to a single IRE1$^{516\text{-}571}$ monomer embedded in a membrane (50% POPC-50% DOPC). Membrane thickness is defined as the distance between the lipid heads of two leaflets. For a coarse-grained membrane, it is defined as the distance between PO4 beads of two leaflets. Bilayer tension increases the membrane surface area and reduces membrane thickness. In the no-tension state, the average membrane thickness is 3.988 nm. The tension of 5 and 15 pN/nm reduced the membrane thickness to 3.94 nm and 3.85 nm, respectively. Compression of -5 pN/nm reduced the membrane surface area

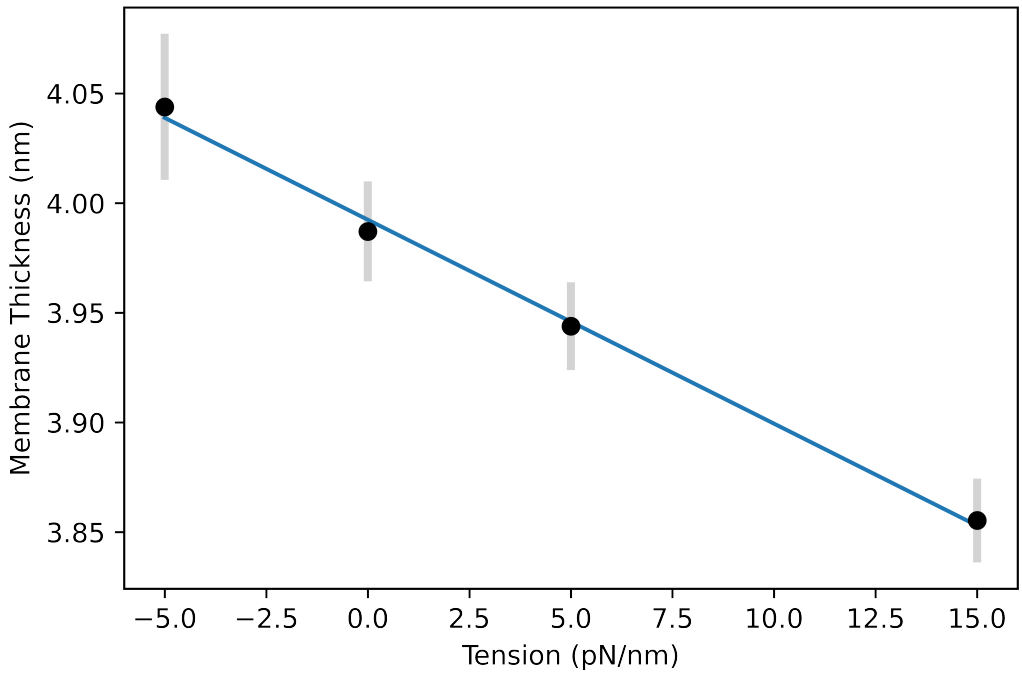

Figure 4.1: Membrane thickness varied linearly with applied bilayer tension. Going from compression of -5 pN/nm to tension of 15 pN/nm decreased the membrane thickness from 40.5 Å to 38.5 Å.

and increased the membrane thickness to 4.04 nm. Fig. 4.1 shows a plot of membrane thickness against bilayer tension. One standard deviation of average membrane thickness is shown by the error bars. This plot shows a linear relationship between membrane thickness and bilayer tension. Observed membrane thickness variation of the tensed membrane is in accordance with the previous finding of mechanosensitivity of DOPC lipid bilayer [Reddy et al., 2012]. Membrane thickness around the IRE1 plays a vital role in IRE1 clustering. To assess the impact of tension on the membrane in greater detail, heatmaps of membrane thickness, shown in Fig. 4.2, were analysed. For no bilayer tension, even though the average membrane thickness is found 3.98 nm, in the vicinity of IRE1$^{516\text{-}571}$ the membrane thickness was depressed to a minimum of 3.720 nm (Fig. 4.2b). Hydrophobic mismatch between the lipids and IRE1$^{516\text{-}571}$ plays a main role in inducing this local membrane compression. The locally depressed

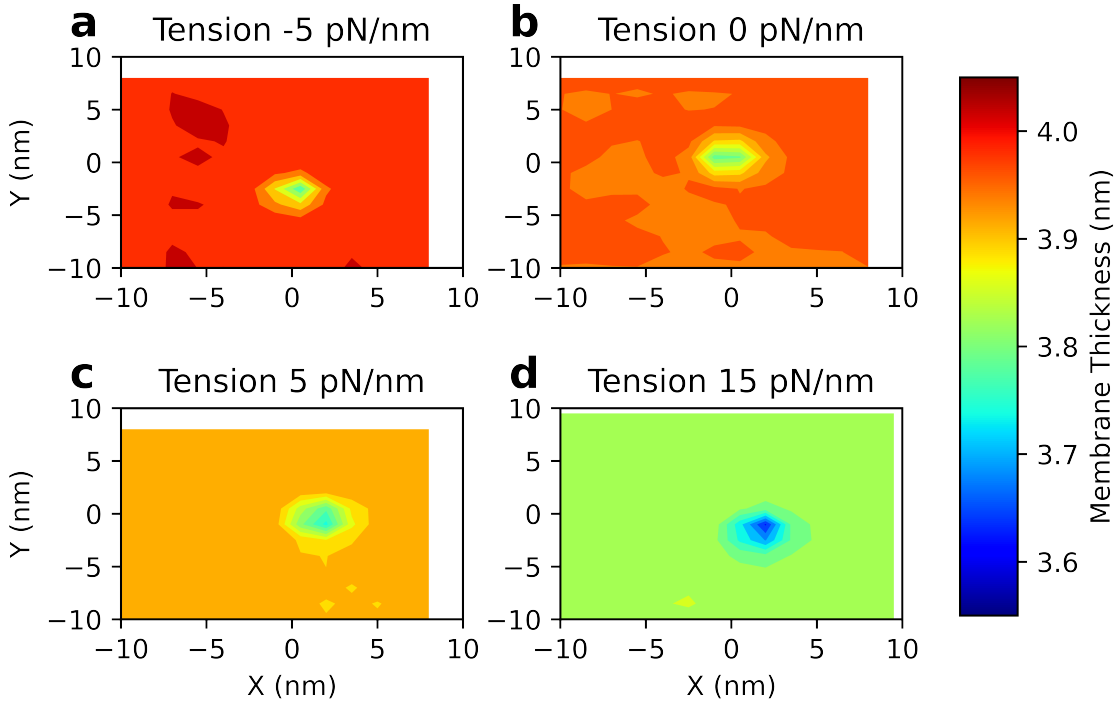

Figure 4.2: Membrane thickness of a single IRE1$^{516\text{-}571}$ monomer-(50%DOPC-50%POPC) complex under various bilayer tensions. (a) Compressing the membrane with -5pN/nm increased the average membrane thickness to 4.044 nm. (b) Under zero tension, the average membrane thickness is 3.987 nm. (c) A bilayer tension of 5 pN/nm reduced the average membrane thickness to 3.944 nm. (d) Bilayer tension 15 pN/nm reduced the avergae membrane thickness to 3.853 nm.

region around IRE1$^{516\text{-}571}$ was also observed in tension and compression due to hydrophobic mismatch but the level of depression was different for each applied load. To quantify and compare the level of compression induced by IRE1 inclusion in tensed membrane, membrane deformation field is analyzed in section 4.2 in detail.

4.1.2 Area per lipid

Tension applied across the membrane surface stretches the membrane, increasing the surface area. On the other hand, compressing the ER reduced the area. To assess the impact of tension on membrane surface area, the area per lipid was calculated. Area per lipid is defined as

$$A_l = \frac{A_{xy}}{N} = \frac{l_x * l_y}{N_\mathrm{p}}, \tag{4.1}$$

where A_l and A represents the area per lipid and membrane surface area, respectively. l_x, l_y are the x and y dimensions of the membrane surface, A. N_p is the total number of lipids. Since bilayer tension changes the membrane surface area, it also changes the area per lipid. Applied tension increases the membrane surface area. Hence, the area per lipid is also increased. For bilayer tension of 5 pN/nm, A_l was increased to 66.5 Å^2 from 65.5 Å^2 for the zero-tension case. The tension of 15 pN/nm further increased the A_l to 69 Å^2. Compression of -5 pN/nm decreased A_l to 64.25 Å^2. By fitting the values of A_l with respect to bilayer tension, I find a linear relationship between them (Fig. 4.3).Fig. 4.3 and Fig. 4.1 indicate that ER bilayer geometry was changed under tension and compression.

4.2 Membrane thickness deformation field and bilayer tension

The membrane deformation field, defined as the difference between the local and far-field (unperturbed) thickness, $u(x, y)$ helps to illustrate the localized membrane compression due to protein inclusions. The membrane deformation field, u(x,y) = h(x,y) − a, where h(x,y) is the membrane thickness at the position (x,y) and a is

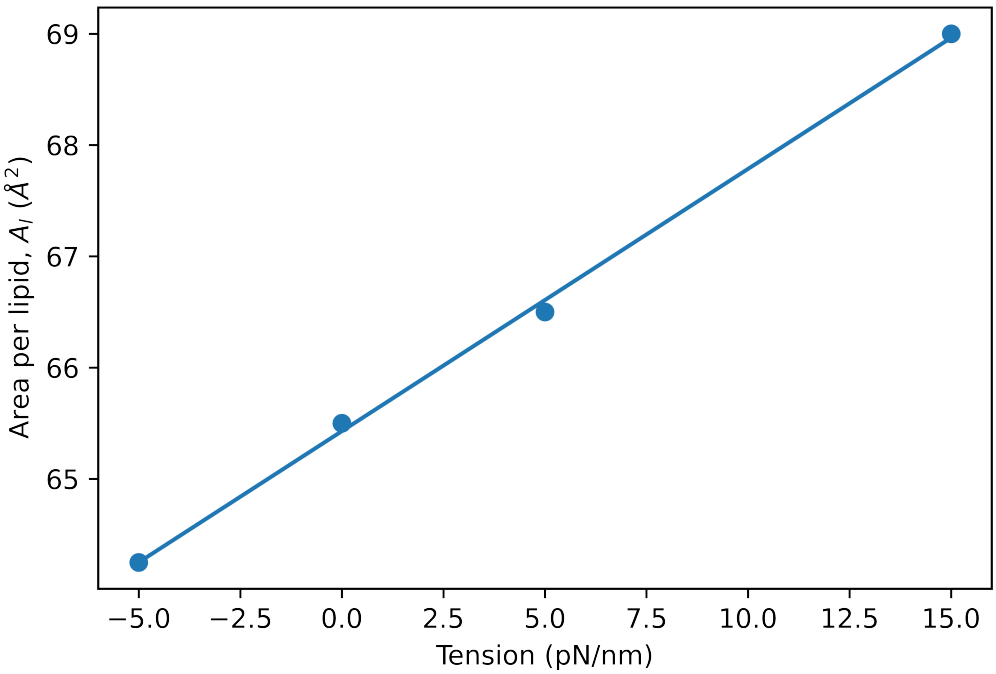

Figure 4.3: Area per lipid shows a linear relationship with bilayer tension. For example, going from compression of -5 pN/nm to tension of 15 pN/nm increased the area per lipid from 64.5 Å^2 to 69 Å^2.

the unperturbed half bilayer thickness measured by averaging the thickness around the perimeter of the simulated bilayer. Fig. 4.4 shows the membrane thickness deformation field around the IRE1$^{516\text{-}571}$ monomer for four cases, (a) compression of -5 pN/nm, (b) zero tension, (c) tension of 5pN/nm and, (d) tension of 15 pN/nm. In Fig. 4.5, the deformation field of IRE1$^{516\text{-}571}$ dimers show similar but more pronounced deformation fields than IRE1$^{516\text{-}571}$ monomers.

4.3 Bilayer tension and crossing angle

The hydrophobic domain of the IRE1$^{516\text{-}571}$ monomer adjusts its orientation in the membrane so that the effective hydrophobic length of IRE1$^{516\text{-}571}$ becomes approximately equal to the bilayer thickness. Additionally, IRE1$^{516\text{-}571}$ has an amphipathic helix that lies at the interface between the ER lumen and the membrane. These

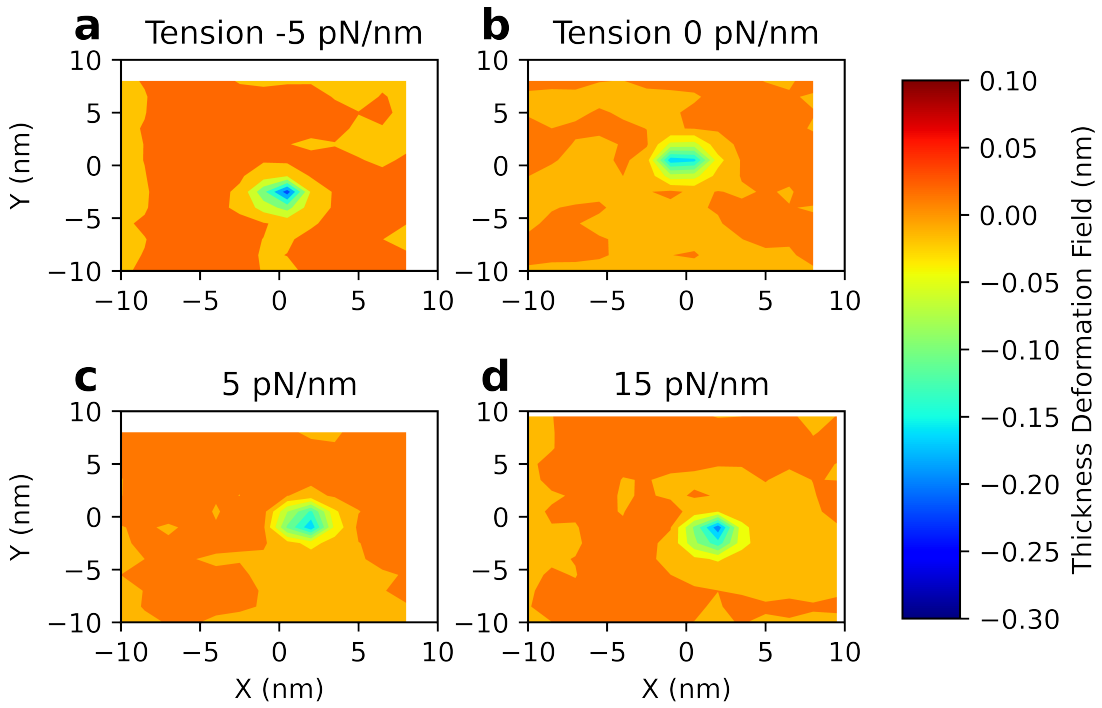

Figure 4.4: Membrane thickness deformation field in the vicinity of IRE1$^{516\text{-}571}$ monomer under application of various bilayer tensions. (a) 5 pN/nm compression was applied to membrane. (b) Membrane thickness deformation field under zero tension. (c) Membrane thickness deformation field under bilayer tension 5 pN/nm. (d) Membrane thickness deformation field under bilayer tension 15 pN/nm.

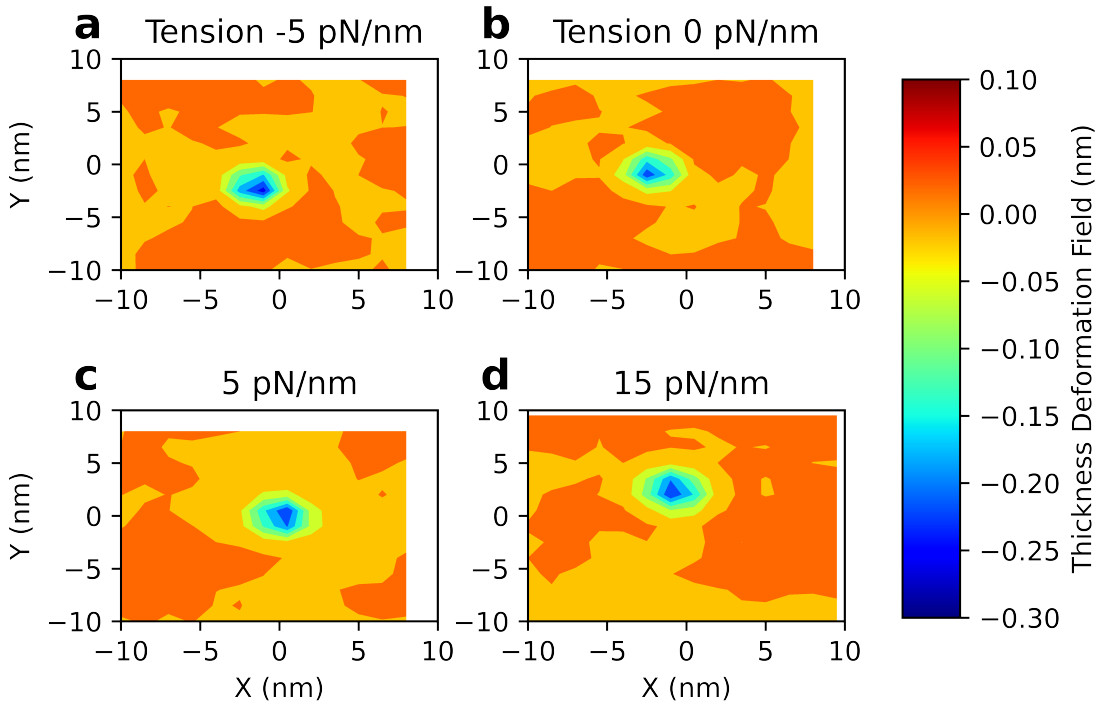

Figure 4.5: Membrane thickness deformation field in the vicinity of IRE1$^{516\text{-}571}$ dimer under application of various bilayer tensions. Membrane depression induced by IRE1$^{516\text{-}571}$ dimer is more pronounced compared to that of IRE1$^{516\text{-}571}$ monomer. (a) Deformation field under compression of 5 pN/nm. (b) Membrane thickness deformation field under zero tension. (c) Membrane thickness deformation field under bilayer tension of 5 pN/nm. (d) Membrane thickness deformation field under bilayer tension of 15 pN/nm.

properties jointly dictate the orientation of IRE1$^{516\text{-}571}$ and the deformation of the membrane around the protein. With no applied tension, IRE1$^{516\text{-}571}$ makes an angle of 45° with the normal of the membrane surface. Tension of 5 pN/nm reduced membrane thickness to 3.944 nm, which forces IRE1$^{516\text{-}571}$ to match its effective hydrophobic length by tilting to be more aligned with the membrane normal. Similarly 15 pN/nm tension increases the tilt angle of the monomer further. On the other hand, membrane compression increases the membrane thickness, reducing the tilt angle. A plot of tilt angle and bilayer tension is shown in Fig. 4.6. Going from compression to tension, the tilt angle increases. While forming a dimer, two monomer will try to form a X-like structure. The angle between the monomer's principal axis is defined as the crossing angle. The crossing angle is approximately equal to twice the inclination angle of IRE1 monomer $^{516\text{-}571}$. A schematic of crossing angle is depicted in inset of the Fig. 4.6. Experimental evidence also showed that two IRE1$^{516\text{-}571}$ monomers form an X-like structure resulting in a crossing angle of 90° in active dimeric form [Väth et al., 2021]. I started my simulations with this active X-like structure of IRE1 dimers. The crossing angle was sustained at 90° for no bilayer tension. The average crossing angle under tension was found to be more than 90° while in compression, it was below 90°. These results show that the membrane-protein dimer complex responds to bilayer tension by both deforming the membrane locally and altering the orientation of the proteins to accommodate the changes in membrane thickness.

4.4 Variation in bilayer tension favors IRE1 dimerization

Bilayer tension applied to the IRE1$^{516\text{-}571}$-membrane complex impacted the free energy of IRE1 dimerization. Fig. 4.7 shows the potential of mean force between IRE1$^{516\text{-}571}$ dimer and monomer upon application of various bilayer tensions. With no externally applied bilayer tension, an energy well depth of -40.5 kJ/mol corresponds to the energy of IRE1$^{516\text{-}571}$ dimerization. However, when a 5 pN/nm compression was applied, the

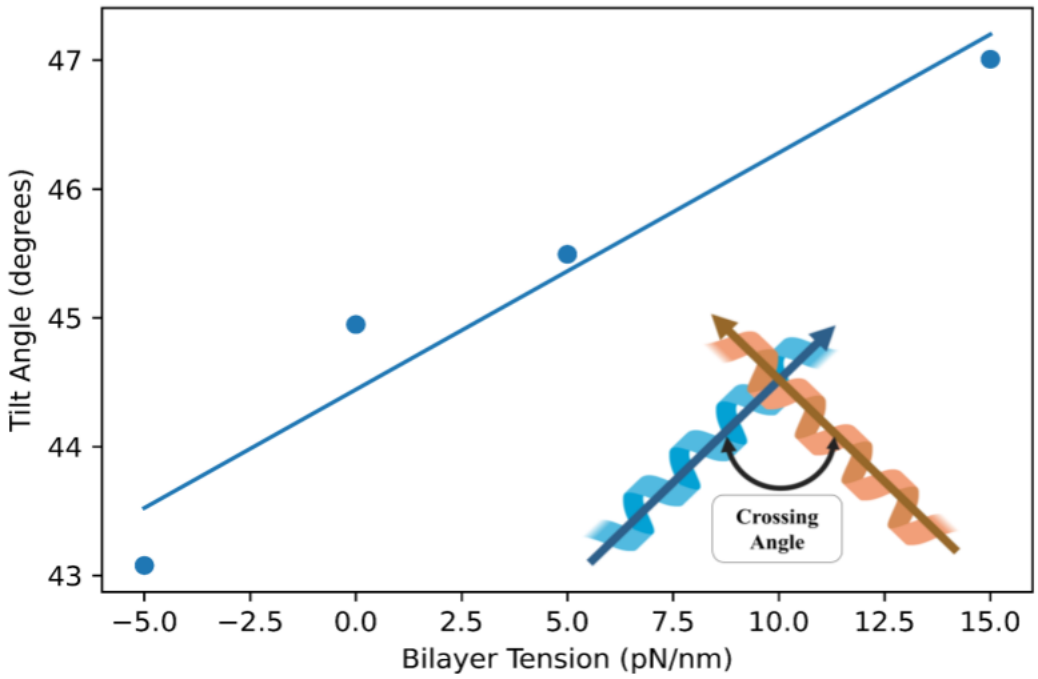

Figure 4.6: Inclination of IRE1$^{516\text{-}571}$ monomer with respect to the normal of membrane surface changed with bilayer tension. Increased bilayer tension increased the inclination towards the membrane surface. In a dimer, IRE1 monomers form a X-like structure and the angle between the two monomers is termed the crossing angle. A schematic of crossing angle is added in the inset.

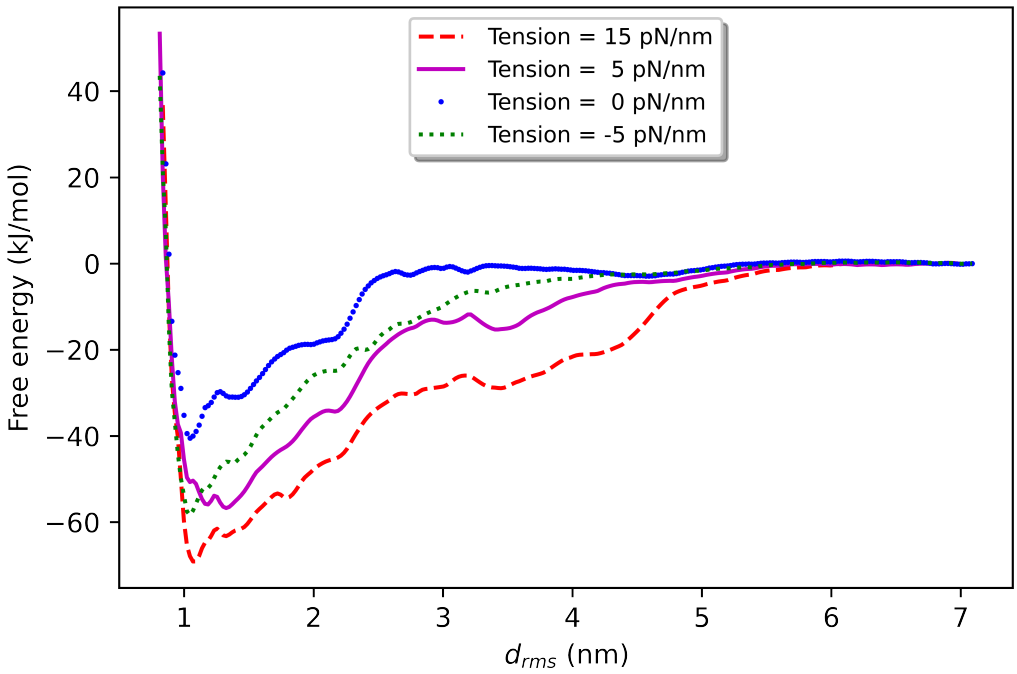

Figure 4.7: Free energy landscapes of IRE1$^{516\text{-}571}$ dimer dissociation as a function d_{rms} upon application of various bilayer tensions. The blue line corresponds to the free energy of IRE1$^{516\text{-}571}$ dimer dissociation at zero bilayer tension with -40.5 kJ/mol. The green line corresponds to the free energy of IRE1$^{516\text{-}571}$ dimer dissociation at compression with a energy well depth of -58 kJ/mol. The magenta line corresponds to the free energy of IRE1$^{516\text{-}571}$ dimer dissociation at the tension of 5 pN/nm with a energy well depth of -56 kJ/mol. The red line corresponds to the free energy of IRE1$^{516\text{-}571}$ dimer dissociation at tension 15 pN/nm with a energy well depth of -73 kJ/mol. Hence, any perturbation in tension increased the well depth of the free energy curve.

energy well depth increased to -58 kJ/mol, demonstrating that more energy is required to dissociate the IRE1$^{516\text{-}571}$ dimer into monomers. As a result, IRE1$^{516\text{-}571}$ dimers are more stable in a compressed membrane than in the zero tension state. Similarly, bilayer tension 5 pN/nm increased energy depth to -56 kJ/mol. Increased well depth both at tension and compression indicates more stable IRE1$^{516\text{-}571}$ dimers than that of no tension state. When the tension was further increased to 15 pN/nm, the energy well deepened to -73 kJ/mol, indicating the most stable IRE1$^{516\text{-}571}$ dimer structure among these four cases. These results show that any change in tension, irrespective of directions (tension or compression), favors IRE1$^{516\text{-}571}$ dimerization.

4.5 Tension modulates stability of UPR-signalling structure

The dissociation constant, K_{d}, of IRE1$^{516\text{-}571}$ dimers at various bilayer tensions can be estimated from the PMFs of IRE1$^{516\text{-}571}$ dimer dissociation. K_{d} was calculated using Equation (3.8). A binding curve shows IRE1 dimer concentration at different concentrations of IRE1 at a specified state (Fig. 4.8). IRE1 dimer ratios are estimated using K_{d} values at different bilayer tensions. In the absence of applied tension, IRE1 dimers dissociate at a rate of 5.94e8 molecules/nm^2. K_{d} estimated from simulation differ from K_{d} determined by experiment because of simplifications of the model. A comparison between experimental K_{d} and computational K_{d} of GpA dimerization has indicated, computed K_{d} is acceptable in spite of having difference [Domański et al., 2017].K_{d} dropped to 5.49e-11 molecules/nm^2 at 5 pN/nm tension. As a result, the binding curve under tension shifts left compared to the zero-tension condition, indicating a greater percentage of IRE1 dimers at the same IRE1 concentration. Similar to the tension, 5 pN/nm compression decreased to K_{d} = 6.32e-11 molecules/nm^2, indicating a larger IRE1 dimer concentration than at zero tension. Bilayer tension of 15 pN/nm further decreased K_{d} to 2.32e-13 molecules/nm^2, exhibiting the highest IRE1 dimer percentage of these four states at 2.32e-13 molecules/nm^2. As a result,

tension and compression increase the concentration of IRE1 in dimeric form. This increased IRE1 dimer concentration would favor IRE1 conformations that initiate the unfolded protein response.

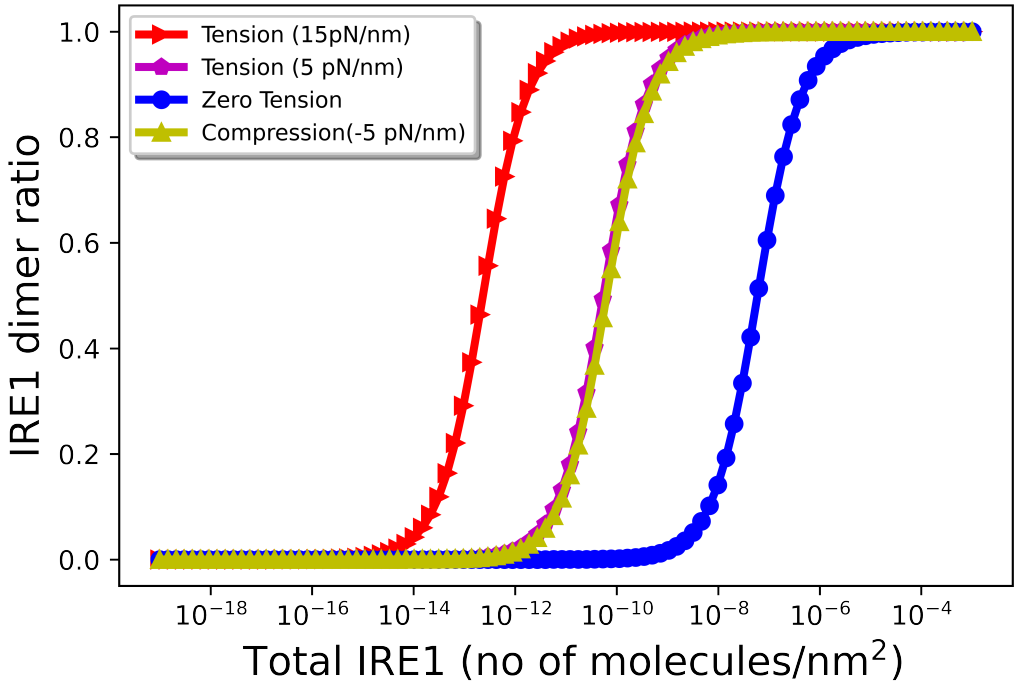

Figure 4.8: Binding curves of IRE1 dimer under application of various bilayer tensions. For a specific IRE1 concentration, a change in bilayer tension altered the concentration of IRE1 dimer. When 5 pN/nm of tension was applied (magenta), the binding curve shifted to the left compared to the no-tension state (blue), which was consistent with an increase in IRE1 dimer concentration at the tensed state. Like the tension of the same magnitude, 5 pN/nm (yellow) compression shifts the curve to the left. Bilayer tension of 15 pN/nm (red) shifts the binding curve even further to the left. Therefore, the ratio of IRE1 found in dimers increases when mechanical loading is applied relative to the zero-tension state. This increased IRE1 dimer concentration would correspond with activation of the UPR.

Chapter 5

Discussion

As expected, in our simulations tension decreases the average membrane thickness, while compression increased the average membrane thickness. Since, in the unperturbed membrane, IRE1 locally reduces the membrane thickness to accommodate hydrophobic mismatch, one might expect externally applied compression to favor dimerization since it would further exacerbate the hydrophobic mismatch of the monomers. Conversely, one might expect tension to favor the monomer state by reducing the hydrophobic mismatch, thereby decreasing the driving force for dimerization. However, our results show that both applied tension and compression enhance the stability of IRE1$^{516\text{-}571}$ dimers. How can this be? In the case of tension, the decrease in membrane thickness leads to a decrease in membrane deformation around the IRE1 monomers. However, the energy required for this (smaller) deformation is greater than that of the untensed membrane because the tension prestrains the membrane, effectively increasing potential energy of system. In compression, despite IRE1 attempting to accommodate the thicker membrane by decreasing its tilt angle, the membrane depression is higher than in untensed membrane due to greater hydrophobic mismatch. This increased deformation also results in a slightly increased potential energy relative to the protein in an unloaded membrane, but does not explain the increase in stability of IRE1 dimers under compression.

To see this more clearly, consider the contribution to the change in energy upon

insertion of a monomer in a tensed membrane with respect to the zero-tension case,

$$\begin{aligned}\Delta E_{\mathrm{p}} &= \frac{K_{\mathrm{t}}}{2}\int\int\left\{\left(\frac{h(x,y)-a_{\gamma 0}}{a_{\gamma 0}}\right)^2-\left(\frac{a-a_{\gamma 0}}{a_{\gamma 0}}\right)^2\right\}dx\,dy, \\ &= \frac{K_{\mathrm{t}}}{2}D_{\mathrm{p}}\end{aligned} \tag{5.1}$$

where $a_{\gamma 0}$ is the unperturbed thickness with no applied tension, and K_{t} is the membrane thickness modulus. D_{p} is the integrated change in membrane thickness for a loaded membrane upon protein insertion The first term of D_{p} represents the strain energy due to the change membrane thickness of inserting a protein into a loaded membrane and the second term represents the work done by the applied tension in changing the thickness of the membrane. Integration is carried out over the whole membrane surface. A plot of ΔE_{p} against applied bilayer tension is shown in Fig. 5.1 (a). Higher ΔE_{p} at higher tension indicates more energy is required to deform the membrane around the IRE1$^{516\text{-}571}$ monomer when the membrane is under tension. In contrast, under compression, ΔE_{p} is lower than that of the zero-tension case. Since insertion of IRE1 takes up space in the membrane, reduces the available space for the lipid molecules. But, due to high bulk modulus of membrane, bilayer is nearly incompressible [Tosh and Collings, 1986, Seemann and Winter, 2003]. Considering lipid volume, V_{p}=constant, or $A_{\mathrm{p}}h$=constant, where A_{p} is the lipid surface area and h is the membrane thickness. By differentiating V_{p}, $A_{\mathrm{p}}\Delta h + \Delta A_{\mathrm{p}} h = 0$ or $\frac{\Delta h}{h} = \frac{\Delta A_{\mathrm{p}}}{-A_{\mathrm{p}}}$. So, any change in membrane thickness is proportional change in area . In case of IRE1 insertion, membrane thickness compression due to insertion is accompanied by the lipid surface area increase around the IRE1 insertion. In the mechanically stressed membrane, the insertion of the protein requires more energy since it must work against the compressive forces. Hence, energy associated with lipid area increase against the applied tension γ can be written as [Watson et al., 2013, Bitbol et al.,

2012]

$$\begin{aligned}\Delta E_\gamma &= \int\int \gamma \left(\frac{h - a_{\gamma 0}}{a_{\gamma 0}}\right) dx\, dy - \int\int \gamma \left(\frac{a - a_{\gamma 0}}{a_{\gamma 0}}\right) dx\, dy \\ &= \int\int \gamma \left(\frac{h - a}{a_{\gamma 0}}\right) dx\, dy\end{aligned} \tag{5.2}$$

where ΔE_γ is the energy due to tension, and $(h(x,y)-a)/a_{\gamma 0}$ indicates area change in terms of membrane thickness. ΔE_γ is calculated by integrating over the whole membrane surface. ΔE_γ for various tensions, calculated from simulations, is shown in Fig. 5.1(a). ΔE_γ is maximal for the membrane under compression and decreases as the compressive force becomes tensile. This suggests that the reason the monomer is less stable in compression is due to tighter packing of lipids which makes it more difficult to insert the protein. On the other hand, the monomer is less stable in tension because of hydrophobic mismatch. To show this, the total elastic energy due to both thickness and area deformations can be calculated as follows

$$\Delta E_\mathrm{t} = \Delta E_\mathrm{p} + \Delta E_\gamma. \tag{5.3}$$

The thickness modulus was found to be 480 pN/nm (see Equation A.2). Fig. 5.1(b) shows ΔE_t as a function of applied tension, calculated from our simulations. ΔE_t increases for both tensed and compressed membranes compared to the zero-tension state. Large uncertainties associated with the estimation of ΔE_t are due to uncertainties in calculating the unperturbed membrane thicknesses in tensed or compressed membranes, similar to other simulations of membrane-protein systems [Argudo et al., 2017]. ΔE_t at different tensions can be used to compare the energy requirement for IRE1$^{516\text{-}571}$ monomer insertion. We see that the continuum model predicts both tension and compression will increase the monomer energy, suggesting a greater driving force for dimerization. Additionally, we see that the driving force for tension is primarily the energy associated with thinning the already-stretched membrane, while the driving force for compression is due to the greater energy needed to create space for the protein in the bilayer. When these contributions are combined, the result is less monomer stability for both compressive and tensile loads.

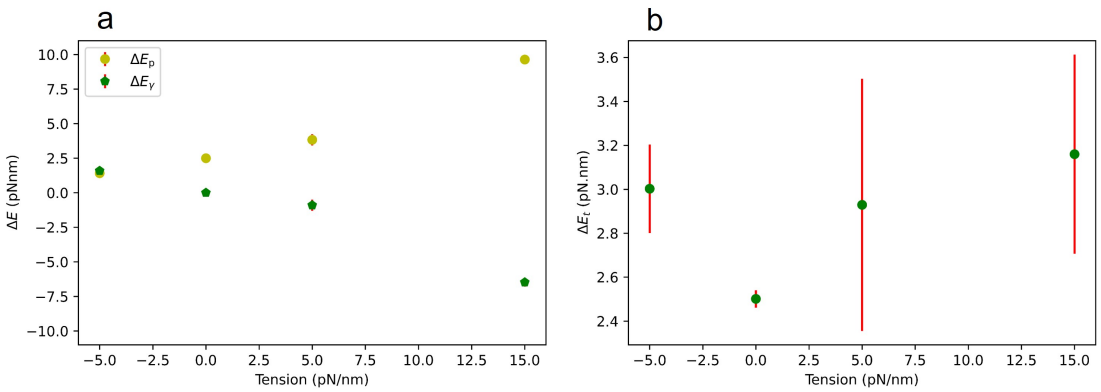

Figure 5.1: The thickness deformation associated with IRE1 monomer insertion in ER (50%DOPC-50%POPC) under various bilayer tensions. Under no externally applied load, IRE1-influenced thickness deformation was found to be 0.01025 nm^2. For applied tensions of 5 and 15 pN/nm thickness deformations of 0.01472 and 0.03729 nm^2 were observed, respectively. On the other hand, compression of 5 pN/nm only slightly increased the thickness deformation relative to the untensed case to 0.01051 nm^2.

In this state of increased instability, IRE1 monomers try to reduce the deformation energy in the membrane by forming dimers. Hence, both applied tension and compression destabilize monomeric IRE1 and favor the formation of dimers. A working model of different orientation of IRE1 dimer is shown in Fig. 5.2. This model depicts the behaviour of the transmembrane domain of IRE1 under various tension. Even though the transmembrane domain of IRE1 has been shown to works as minimalistic sensor for UPR activation, this model is unable to capture the orientation of the kinase portion of IRE1. Molecular dynamics simulation of full length IRE1 under tension might provide more inside into full conformation state of IRE1.

In cells, IRE1 forms large oligomeric signalling clusters. While my simulations only consider the relative stability of monomers and dimers, I expect that larger signalling clusters would be even more favorable upon mechanical perturbations of the membrane. Since the driving force of dimerization in our study results from decreasing the total deformation of the membrane by overlapping the deformation fields of each monomer, it is reasonable to suppose that further decreasing the total area by forming larger oligomeric clusters would be even more favorable. Hence, our

study predicts that mechanical perturbations to the ER membrane could lead to the formation of active IRE1 signalling clusters and activation of the UPR in the absence of misfolded protein stress. This is similar to how lipid composition has been shown to regulate the UPR independent of proteotoxic stress.

Despite the extensive simulations used to establish the mechanosensitivity of $IRE1^{516\text{-}571}$ in this work, I am unaware of any experimental evidence showing direct activation of the UPR by mechanical forces. Due to computational expense, our study was limited to the transmembrane section of IRE1. Since both the lumenal and cytosolic portions of IRE1 interact with other IRE1 molecules in oligomers, it is possible that full-length IRE1 molecules may behave differently. However, activation of the IRE1 signalling pathway upon lipid compositional changes lends credence to the ability of the transmembrane section of IRE1 to promote clustering in cell. To confirm the predicted mechanical regulation of the UPR, experimental measurements of full-length IRE1 in tensed membranes are needed.

Sensitivity of IRE1 to membrane tension provides another example of unfolded-protein-independent UPR activation. The tension in the ER membrane would be expected to change as the pressure within the ER changes, for example due to osmotic stress or from an influx of nascent proteins, as well as from cytoskeletal forces applied at anchoring points within the ER membrane. The mechanosensitiviy of IRE1 would allow cells to monitor and respond to these perturbations. Also, Climp63, which has been identified as marker for ER shape, can be used to modulate the the spacing between ER sheet and potentially impact tension in the ER. A further experimental study of concentration of Climp63, ER tension and IRE1 concentration can provide more insight into UPR activation in mechanically stressed cell. Lastly, since the transmembrane domain of PERK is very similar to that of IRE1, and both activate by clustering in the ER membrane, it seems plausible that the PERK signalling pathway may also be sensitive to ER bilayer tension, although further computational and experimental work would be required to confirm this.

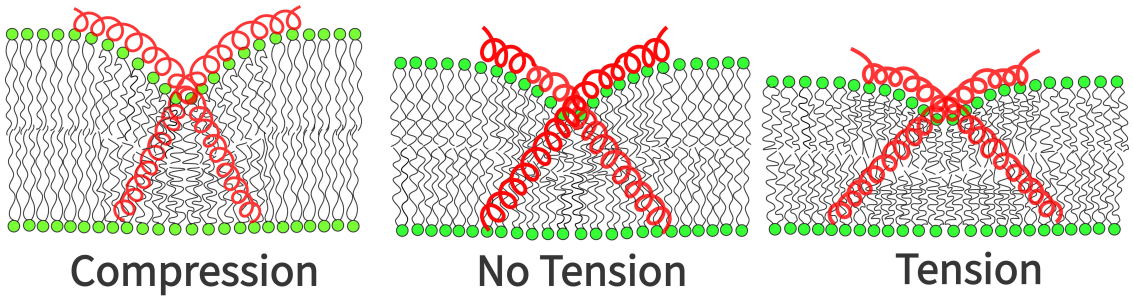

Figure 5.2: A schematic diagram of $IRE1^{516\text{-}571}$ dimer under various bilayer tensions. Lipid heads and tails are represented with green circles and black lines, respectively. $IRE1^{516\text{-}571}$ monomers are represented by red helices. With no tension applied, $IRE1^{516\text{-}571}$ dimer forms a X-like configuration with crossing angle 90°. Amphipathic helix of $IRE1^{516\text{-}571}$ sits on top surface of ER because of its hydrophilic face. Tensing the ER will decrease the membrane thickness. $IRE1^{516\text{-}571}$ matches its effective hydrophobic length with the membrane thickness by tilting towards membrane surface and keeping the hydrophilic face of amphipathic helix of $IRE1^{516\text{-}571}$ on the top surface of lipids. This changed formation of $IRE1^{516\text{-}571}$ dimer results in crossing angle greater than 90° and increases the energy related to the thickness of the membrane around the monomer. On the other hand, increased membrane thickness under compression causes $IRE1^{516\text{-}571}$ to adopt a less inclined orientation with a crossing angle less than 90°. The compression of the lipids makes the monomer less stable do to the in-plane strain needed to insert the protein, also driving dimerization.

Chapter 6

Conclusion

In this research, we used coarse-grained molecular dynamics simulation to examine the effect of bilayer tension on IRE1 dimerization in the ER. Bilayer tension's mechanical interference with the ER environment alters bulk physical properties like membrane thickness and area per lipid. Tension reduced membrane thickness and expanded area per lipid by stretching the membrane surface. Compression, on the other hand, resulted in a thicker membrane and a smaller area per lipid. IRE1 dimers were found to be more stable under either tension or compression compared to the case in which no load was applied, as evidenced by the greater free-energy well depth between the dimer and monomer states. Under tension, this increased stability can be explained by the increased energy required to locally depress the membrane around the monomer. Dimerization releases some of this strain energy by allowing the depressions of each monomer to overlap. The energy released by this process when the membrane is under tension is greater than when no load is applied. The driving force for dimerization when the membrane is under compression is similarly the result a release in strain energy of the membrane by bringing two monomers into contact. However, in compression, the in-plane deformation, which destabilizes the monomer by more tightly packing lipids, drives dimerization. By stabilizing the dimer, both tension and compression raise the IRE1 dimer percentage at a specific IRE1 concentration, which would activate the UPR. Therefore, this study demonstrates a novel

mechanisms for controlling UPR activation by through mechanic perturbations to the ER membrane. Future extension of this study could be use of artificial intelligence to discover computationally efficient reaction coordinate to explore more long range-phenomena of IRE1 clustering. A multiscale modeling of IRE1 clustering will also provide more insight on the IRE1 activated UPR. Molecular dynamics simulation of PERK, another ER stress sensor under tension/compression can reveal detailed the molecular mechanism of tension activated UPR.

Bibliography

B. Alberts, A. Johnson, J. Lewis, M. Raff, K. Roberts, and P. Walter. *Molecular Biology of the Cell*. Garland Science, New York, 6th edition, 2017. ISBN 9780815344643.

V. Allen and R. David. The endoplasmic reticulum stress response in the pancreatic β-cell. *Diabetes, Obesity & Metabolism*, 12 Suppl 2(SUPPL. 2):48–57, 2010. doi: 10.1111/j.1463-1326.2010.01271.x.

D. Argudo, N. P. Bethel, F. V. Marcoline, C. W. Wolgemuth, and M. Grabe. New continuum approaches for determining protein-induced membrane deformations. *Biophysical Journal*, 112(10):2159–2172, May 2017. doi: 10.1016/j.bpj.2017.03.040.

K. Ben M'barek, D. Ajjaji, A. Chorlay, S. Vanni, L. Forêt, and A. R. Thiam. ER Membrane Phospholipids and Surface Tension Control Cellular Lipid Droplet Formation. *Developmental Cell*, 41(6):591–604.e7, Jun 2017. doi: 10.1016/j.devcel.2017.05.012.

A. Bertolotti, Y. Zhang, L. M. Hendershot, H. P. Harding, and D. Ron. Dynamic interaction of BiP and ER stress transducers in the unfolded-protein response. *Nature Cell Biology*, 2(6):326–332, May 2000. doi: 10.1038/35014014.

A.-F. Bitbol, D. Constantin, and J.-B. Fournier. Bilayer elasticity at the nanoscale: The need for new terms. *PLOS ONE*, 7(11):1–19, Nov 2012. doi: 10.1371/journal.pone.0048306.

I. Braakman and D. N. Hebert. Protein folding in the endoplasmic reticulum. *Cold Spring Harbor Perspectives in Biology*, 5(5), 2013. doi: 10.1101/cshperspect.a013201.

B. R. Brooks, C. L. Brooks, A. D. Mackerell, L. Nilsson, R. J. Petrella, B. Roux, Y. Won, G. Archontis, C. Bartels, S. Boresch, A. Caflisch, L. Caves, Q. Cui, A. R. Dinner, M. Feig, S. Fischer, J. Gao, M. Hodoscek, W. Im, K. Kuczera, T. Lazaridis, J. Ma, V. Ovchinnikov, E. Paci, R. W. Pastor, C. B. Post, J. Z. Pu, M. Schaefer, B. Tidor, R. M. Venable, H. L. Woodcock, X. Wu, W. Yang, D. M. York, and M. Karplus. CHARMM: The biomolecular simulation program. *Journal of Computational Chemistry*, 30(10):1545–1614, Jul 2009. doi: 10.1002/jcc.21287.

M. F. Brown. Modulation of rhodopsin function by properties of the membrane bilayer. *Chemistry and Physics of Lipids*, 73(1-2):159–180, Sep 1994. doi: 10.1016/0009-3084(94)90180-5.

M. Calfon, H. Zeng, F. Urano, J. H. Till, S. R. Hubbard, H. P. Harding, S. G. Clark, and D. Ron. IRE1 couples endoplasmic reticulum load to secretory capacity by processing the XBP-1 mRNA. *Nature*, 415(6867):92–96, Jan 2002. doi: https://doi.org/10.1038/415092a.

D. E. Clapham. Calcium Signaling. *Cell*, 131(6):1047–1058, Dec 2007. doi: 10.1016/j.cell.2007.11.028.

R. Covino, G. Hummer, and R. Ernst. Integrated Functions of Membrane Property Sensors and a Hidden Side of the Unfolded Protein Response. *Molecular Cell*, 71 (3):458–467, 2018. doi: 10.1016/j.molcel.2018.07.019.

J. S. Cox and W. Peter. A novel mechanism for regulating activity of a transcription factor that controls the unfolded protein response. *Cell*, 87(3):391–404, Nov 1996. doi: 10.1016/s0092-8674(00)81360-4.

J. S. Cox, C. E. Shamu, and P. Walter. Transcriptional induction of genes encoding endoplasmic reticulum resident proteins requires a transmembrane protein kinase. *Cell*, 73(6):1197–1206, Jun 1993. doi: 10.1016/0092-8674(93)90648-a.

E. Darve, D. Rodríguez-Gómez, and A. Pohorille. Adaptive biasing force method for scalar and vector free energy calculations. *The Journal of Chemical Physics*, 128 (14), Apr 2008. ISSN 0021-9606. doi: 10.1063/1.2829861. 144120.

E. Decio L and C. Miriam. ER stress in pancreatic beta cells: the thin red line between adaptation and failure. *Science Signaling*, 3(110), Feb 2010. doi: 10.1126/scisignal.3110pe7.

J. Domański, G. Hedger, R. B. Best, P. J. Stansfeld, and M. S. Sansom. Convergence and Sampling in Determining Free Energy Landscapes for Membrane Protein Association. *The Journal of Physical Chemistry B*, 121(15):3364–3375, 2017. doi: 10.1021/acs.jpcb.6b08445.

W. E, W. Ren, and E. Vanden-Eijnden. String method for the study of rare events. *Phys. Rev. B*, 66:052301, Aug 2002. doi: 10.1103/PhysRevB.66.052301.

J. R. Elliott, D. Needham, J. P. Dilger, and D. A. Haydon. The effects of bilayer thickness and tension on gramicidin single-channel lifetime. *Biochimica et Biophysica Acta*, 735(1):95–103, Oct 1983. doi: 10.1016/0005-2736(83)90264-x.

A. R. English and G. K. Voeltz. Endoplasmic reticulum structure and interconnections with other organelles. *Cold Spring Harbor Perspectives in Biology*, 5(4): a013227–a013227, Apr 2013. doi: 10.1101/cshperspect.a013227.

A. R. English, N. Zurek, and G. K. Voeltz. Peripheral er structure and function. *Current Opinion in Cell Biology*, 21(4):596–602, Aug 2009. doi: 10.1016/j.ceb.2009.04.004.

P. Fagone and S. Jackowski. Membrane phospholipid synthesis and endoplasmic reticulum function. *Journal of Lipid Research*, 50(SUPPL.):S311, Apr 2009. doi: 10.1194/jlr.R800049-jlr200.

G. Fiorin, M. L. Klein, and J. Hénin. Using collective variables to drive molecular dynamics simulations. *Molecular Physics*, 111(22-23):3345–3362, 2013. doi: 10.1080/00268976.2013.813594.

J. R. Friedman and G. K. Voeltz. The ER in 3d: a multifunctional dynamic membrane network. *Trends in Cell Biology*, 21(12):709–717, Dec 2011. doi: 10.1016/j.tcb.2011.07.004.

B. M. Gardner, D. Pincus, K. Gotthardt, C. M. Gallagher, and P. Walter. Endoplasmic reticulum stress sensing in the unfolded protein response. *Cold Spring Harbor Perspectives in Biology*, 5(3):a013169–a013169, Feb 2013. doi: 10.1101/cshperspect.a013169.

A. Grossfield. Wham: the weighted histogram analysis method, version 2.0.11.

H. Grubmüller. Predicting slow structural transitions in macromolecular systems: Conformational flooding. *Physical Review E*, 52:2893–2906, Sep 1995. doi: 10.1103/PhysRevE.52.2893.

R. Guixà-González, I. Rodriguez-Espigares, J. M. Ramírez-Anguita, P. Carrió-Gaspar, H. Martinez-Seara, T. Giorgino, and J. Selent. MEMBPLUGIN: studying membrane complexity in VMD. *Bioinformatics*, 30(10):1478–1480, Jan 2014. doi: 10.1093/bioinformatics/btu037.

H. Gökhan S. Endoplasmic reticulum stress and the inflammatory basis of metabolic disease. *Cell*, 140(6):900–917, 2010. doi: 10.1016/j.cell.2010.02.034.

K. Halbleib, K. Pesek, R. Covino, H. F. Hofbauer, D. Wunnicke, I. Hänelt, G. Hum-

mer, and R. Ernst. Activation of the Unfolded Protein Response by Lipid Bilayer Stress. *Molecular Cell*, 67(4):673–684.e8, 2017. doi: 10.1016/j.molcel.2017.06.012.

D. Hamelberg, J. Mongan, and J. A. McCammon. Accelerated molecular dynamics: A promising and efficient simulation method for biomolecules. *The Journal of Chemical Physics*, 120(24):11919–11929, 06 2004. ISSN 0021-9606. doi: 10.1063/1.1755656.

F. U. Hartl. Molecular chaperones in cellular protein folding. *Nature*, 381(6583): 571–580, Jun 1996. doi: 10.1038/381571a0.

D. N. Hebert, S. C. Garman, and M. Molinari. The glycan code of the endoplasmic reticulum: Asparagine-linked carbohydrates as protein maturation and quality-control tags. *Trends in Cell Biology*, 15(7):364–370, Jul 2005. doi: 10.1016/j.tcb.2005.05.007.

C. Hetz. The unfolded protein response: controlling cell fate decisions under ER stress and beyond. *Nature Reviews Molecular Cell Biology 2012 13:2*, 13(2):89–102, Jan 2012. doi: 10.1038/nrm3270.

C. Hetz and S. Saxena. ER stress and the unfolded protein response in neurodegeneration. *Nature reviews. Neurology*, 13(8):477–491, Aug 2017. doi: 10.1038/nrneurol.2017.99.

P. C. Hsu, B. M. Bruininks, D. Jefferies, P. Cesar Telles de Souza, J. Lee, D. S. Patel, S. J. Marrink, Y. Qi, S. Khalid, and W. Im. Charmm-gui martini maker for modeling and simulation of complex bacterial membranes with lipopolysaccharides. *Journal of Computational Chemistry,*, 38(27):2354–2363, 2017. doi: 10.1002/jcc.24895.

J. Hu, W. A. Prinz, and T. A. Rapoport. Weaving the web of ER tubules. *Cell*, 147 (6):1226–1231, Dec 2011. doi: 10.1016/j.cell.2011.11.022.

W. Humphrey, A. Dalke, and K. Schulten. VMD – Visual Molecular Dynamics. *Journal of Molecular Graphics*, 14:33–38, 1996.

S. Jo, T. Kim, V. G. Iyer, and W. Im. CHARMM-GUI: A web-based graphical user interface for CHARMM. *Journal of Computational Chemistry*, 29(11):1859–1865, Aug 2008. doi: 10.1002/jcc.20945.

S. Jo, J. B. Lim, J. B. Klauda, and W. Im. CHARMM-GUI membrane builder for mixed bilayers and its application to yeast membranes. *Biophysical Journal*, 97(1): 50–58, Jul 2009. doi: 10.1016/j.bpj.2009.04.013.

J. Killian. Hydrophobic mismatch between proteins and lipids in membranes. *Biochimica et Biophysica Acta (BBA) - Reviews on Biomembranes*, 1376(3):401–416, Nov 1998. doi: 10.1016/s0304-4157(98)00017-3.

J. A. Killian and T. K. Nyholm. Peptides in lipid bilayers: the power of simple models. *Current Opinion in Structural Biology*, 16(4):473–479, Aug 2006. doi: 10.1016/j.sbi.2006.06.007.

J. B. Klauda, R. M. Venable, J. A. Freites, J. W. O'Connor, D. J. Tobias, C. Mondragon-Ramirez, I. Vorobyov, A. D. MacKerell, and R. W. Pastor. Update of the CHARMM all-atom additive force field for lipids: Validation on six lipid types. *The Journal of Physical Chemistry. B*, 114(23):7830, Jun 2010. doi: 10.1021/jp101759q.

A. V. Korennykh, P. F. Egea, A. A. Korostelev, J. Finer-Moore, C. Zhang, K. M. Shokat, R. M. Stroud, and P. Walter. The unfolded protein response signals through high-order assembly of ire1. *Nature*, 457(7230):687–693, Dec 2008. doi: 10.1038/nature07661.

M. M. Kozlov and L. V. Chernomordik. Membrane tension and membrane fusion.

Current Opinion in Structural Biology, 33:61–67, Aug 2015. doi: 10.1016/j.sbi.2015.07.010.

N. Krahmer, R. V. Farese, and T. C. Walther. Balancing the fat: lipid droplets and human disease. *EMBO Molecular Medicine*, 5(7):973–983, Jun 2013. doi: 10.1002/emmm.201100671.

A. Laio and M. Parrinello. Escaping free-energy minima. *Proceedings of the National Academy of Sciences*, 99(20):12562–12566, 2002. doi: 10.1073/pnas.202427399.

J. Lee, X. Cheng, J. M. Swails, M. S. Yeom, P. K. Eastman, J. A. Lemkul, S. Wei, J. Buckner, J. C. Jeong, Y. Qi, S. Jo, V. S. Pande, D. A. Case, C. L. Brooks, A. D. MacKerell, J. B. Klauda, and W. Im. CHARMM-GUI Input Generator for NAMD, GROMACS, AMBER, OpenMM, and CHARMM/OpenMM Simulations Using the CHARMM36 Additive Force Field. *Journal of Chemical Theory and Computation*, 12(1):405–413, Jan 2016. doi: 10.1021/acs.jctc.5b00935.

J. Lee, D. S. Patel, J. Ståhle, S. J. Park, N. R. Kern, S. Kim, J. Lee, X. Cheng, M. A. Valvano, O. Holst, Y. A. Knirel, Y. Qi, S. Jo, J. B. Klauda, G. Widmalm, and W. Im. CHARMM-GUI Membrane Builder for Complex Biological Membrane Simulations with Glycolipids and Lipoglycans. *Journal of Chemical Theory and Computation*, 15(1):775–786, Jan 2019. doi: 10.1021/acs.jctc.8b01066.

Q. Liao. *Chapter Four - Enhanced sampling and free energy calculations for protein simulations*, volume 170 of *Progress in Molecular Biology and Translational Science*. Academic Press, 2020. doi: https://doi.org/10.1016/bs.pmbts.2020.01.006.

J. H. Lin, H. Li, D. Yasumura, H. R. Cohen, C. Zhang, B. Panning, K. M. Shokat, M. M. LaVail, and P. Walter. IRE1 signaling affects cell fate during the unfolded protein response. *Science*, 318(5852):944–949, Nov 2007. doi: 10.1126/science.1146361.

H. Lu and K. Schulten. Steered molecular dynamics simulations of force-induced protein domain unfolding. *Proteins: Structure, Function, and Bioinformatics*, 35 (4):453–463, 1999. doi: https://doi.org/10.1002/(SICI)1097-0134(19990601)35:4⟨453::AID-PROT9⟩3.0.CO;2-M.

L. Maragliano and E. Vanden-Eijnden. A temperature accelerated method for sampling free energy and determining reaction pathways in rare events simulations. *Chemical Physics Letters*, 426(1):168–175, 2006. ISSN 0009-2614. doi: https://doi.org/10.1016/j.cplett.2006.05.062.

S. J. Marrink, H. J. Risselada, S. Yefimov, D. P. Tieleman, and A. H. De Vries. The MARTINI force field: Coarse grained model for biomolecular simulations. *The Journal of Physical Chemistry B*, 111(27):7812–7824, 2007. doi: 10.1021/jp071097f.

K. Morl, W. Ma, M.-J. Gething, and J. Sambrook. A transmembrane protein with a cdc2CDC28-related kinase activity is required for signaling from the ER to the nucleus. *Cell*, 74(4):743–756, Aug 1993. doi: 10.1016/0092-8674(93)90521-q.

O. G. Mouritsen and M. Bloom. Mattress model of lipid-protein interactions in membranes. *Biophysical Journal*, 46(2):141–153, Aug 1984. doi: 10.1016/S0006-3495(84)84007-2.

H. S. Muddana, R. R. Gullapalli, E. Manias, and P. J. Butler. Atomistic simulation of lipid and DiI dynamics in membrane bilayers under tension. *Physical Chemistry Chemical Physics*, 13(4):1368, Jan 2011. doi: 10.1039/c0cp00430h.

E. Perozo, A. Kloda, D. M. Cortes, and B. Martinac. Physical principles underlying the transduction of bilayer deformation forces during mechanosensitive channel gating. *Nature Structural Biology*, 9(9):696–703, 2002. doi: 10.1038/nsb827.

J. C. Phillips, D. J. Hardy, J. D. Maia, J. E. Stone, J. V. Ribeiro, R. C. Bernardi, R. Buch, G. Fiorin, J. Hénin, W. Jiang, R. McGreevy, M. C. Melo, B. K. Radak,

R. D. Skeel, A. Singharoy, Y. Wang, B. Roux, A. Aksimentiev, Z. Luthey-Schulten, L. V. Kalé, K. Schulten, C. Chipot, and E. Tajkhorshid. Scalable molecular dynamics on CPU and GPU architectures with NAMD. *Journal of Chemical Physics*, 153(4):044130, Jul 2020. doi: 10.1063/5.0014475.

L. Pineau, J. Colas, S. Dupont, L. Beney, P. Fleurat-Lessard, J. M. Berjeaud, T. Bergès, and T. Ferreira. Lipid-Induced ER Stress: Synergistic Effects of Sterols and Saturated Fatty Acids. *Traffic*, 10(6):673–690, Jun 2009. ISSN 1600-0854. doi: 10.1111/j.1600-0854.2009.00903.x.

B. Pontes, P. Monzo, and N. C. Gauthier. Membrane tension: A challenging but universal physical parameter in cell biology. *Seminars in Cell & Developmental Biology*, 71:30–41, 2017. doi: https://doi.org/10.1016/j.semcdb.2017.08.030.

T. Promlek, Y. Ishiwata-Kimata, M. Shido, M. Sakuramoto, K. Kohno, and Y. Kimata. Membrane aberrancy and unfolded proteins activate the endoplasmic reticulum stress sensor Ire1 in different ways. *Molecular Biology of the Cell*, 22(18): 3520–3532, Sep 2011. ISSN 1939-4586. doi: 10.1091/mbc.e11-04-0295.

T. A. Rapoport. Protein translocation across the eukaryotic endoplasmic reticulum and bacterial plasma membranes. *Nature*, 450(7170):663–669, Nov 2007. doi: 10.1038/nature06384.

W. Rawicz, K. C. Olbrich, T. McIntosh, D. Needham, and E. A. Evans. Effect of chain length and unsaturation on elasticity of lipid bilayers. *Biophysical Journal*, 79(1):328, 2000. doi: 10.1016/s0006-3495(00)76295-3.

A. S. Reddy, D. T. Warshaviak, and M. Chachisvilis. Effect of membrane tension on the physical properties of dopc lipid bilayer membrane. *Biochimica et Biophysica Acta (BBA) - Biomembranes*, 1818(9):2271–2281, 2012. doi: https://doi.org/10.1016/j.bbamem.2012.05.006.

D. W. Reid and C. V. Nicchitta. Diversity and selectivity in mRNA translation on the endoplasmic reticulum. *Nature Reviews Molecular Cell Biology*, 16(4):221–231, Apr 2015. doi: 10.1038/nrm3958.

D. Ron and P. Walter. Signal integration in the endoplasmic reticulum unfolded protein response. *Nature Reviews Molecular Cell Biology*, 8(7):519–529, Jul 2007. doi: 10.1038/nrm2199.

U. Schmidt, G. Guigas, and M. Weiss. Cluster formation of transmembrane proteins due to hydrophobic mismatching. *Physical Review Letters*, 101(12):1–4, 2008. doi: 10.1103/physrevlett.101.128104.

H. Seemann and R. Winter. Volumetric properties, compressibilities and volume fluctuations in phospholipid-cholesterol bilayers. *Zeitschrift für Physikalische Chemie*, 217(7):831–846, 2003. doi: doi:10.1524/zpch.217.7.831.20388.

Y. Shibata, G. K. Voeltz, and T. A. Rapoport. Rough sheets and smooth tubules. *Cell*, 126(3):435–439, Aug 2006. doi: 10.1016/j.cell.2006.07.019.

C. Sidrauski and P. Walter. The transmembrane kinase ire1p is a site-specific endonuclease that initiates mRNA splicing in the unfolded protein response. *Cell*, 90 (6):1031–1039, Sep 1997. doi: 10.1016/s0092-8674(00)80369-4.

M. H. Smith, H. L. Ploegh, and J. S. Weissman. Road to ruin: Targeting proteins for degradation in the endoplasmic reticulum. *Science*, 334(6059):1086–1090, Nov 2011. doi: 10.1126/science.1209235.

M. M. Sperotto and O. G. Mouritsen. Dependence of lipid membrane phase transition temperature on the mismatch of protein and lipid hydrophobic thickness. *European Biophysics Journal*, 16(1):1–10, May 1988. doi: 10.1007/bf00255320.

M. M. Sperotto, J. H. Ipsen, and O. G. Mouritsen. Theory of protein-induced lateral

phase separation in lipid membranes. *Cell Biophysics*, 14(1):79–95, Feb 1989. doi: 10.1007/bf02797393.

I. D. Stigliano, S. G. Alculumbre, C. A. Labriola, A. J. Parodi, and C. D'Alessio. Glucosidase II andin/i-glycan mannose content regulate the half-lives of monoglucosylated species in vivo. *Molecular Biology of the Cell*, 22(11):1810–1823, Jun 2011. doi: 10.1091/mbc.e11-01-0019.

Y. Sugita and Y. Okamoto. Replica-exchange molecular dynamics method for protein folding. *Chemical Physics Letters*, 314(1):141–151, 1999. ISSN 0009-2614. doi: https://doi.org/10.1016/S0009-2614(99)01123-9.

M. A. Surma, C. Klose, D. Peng, M. Shales, C. Mrejen, A. Stefanko, H. Braberg, D. E. Gordon, D. Vorkel, C. S. Ejsing, R. Farese, K. Simons, N. J. Krogan, and R. Ernst. A Lipid E-MAP Identifies Ubx2 as a Critical Regulator of Lipid Saturation and Lipid Bilayer Stress. *Molecular Cell*, 51(4):519–530, Aug 2013. ISSN 1097-2765. doi: 10.1016/J.molcel.2013.06.014.

E. Szegezdi, S. E. Logue, A. M. Gorman, and A. Samali. Mediators of endoplasmic reticulum stress-induced apoptosis. *EMBO Reports*, 7(9):880, Sep 2006. doi: 10.1038/sj.embor.7400779.

G. Thibault, G. Shui, W. Kim, G. C. McAlister, N. Ismail, S. P. Gygi, M. R. Wenk, and D. T. Ng. The membrane stress response buffers lethal effects of lipid disequilibrium by reprogramming the protein homeostasis network. *Molecular Cell*, 48(1):16–27, Oct 2012. ISSN 1097-4164. doi: 10.1016/j.molcel.2012.08.016.

G. Torrie and J. Valleau. Nonphysical sampling distributions in monte carlo free-energy estimation: Umbrella sampling. *Journal of Computational Physics*, 23(2):187–199, 1977. ISSN 0021-9991. doi: https://doi.org/10.1016/0021-9991(77)90121-8.

R. E. Tosh and P. J. Collings. High pressure volumetric measurements in dipalmitoylphosphatidylcholine bilayers. *Biochimica et Biophysica Acta (BBA) - Biomembranes*, 859(1):10–14, 1986. ISSN 0005-2736. doi: https://doi.org/10.1016/0005-2736(86)90312-3.

K. Väth, C. Mattes, J. Reinhard, R. Covino, H. Stumpf, G. Hummer, and R. Ernst. Cysteine cross-linking in native membranes establishes the transmembrane architecture of Ire1. *Journal of Cell Biology*, 220(8), 2021. doi: 10.1083/jcb.202011078.

S. S. Vembar and J. L. Brodsky. One step at a time: endoplasmic reticulum-associated degradation. *Nature Reviews Molecular Cell Biology*, 9(12):944–957, Nov 2008. doi: 10.1038/nrm2546.

G. K. Voeltz and W. A. Prinz. Sheets, ribbons and tubules — how organelles get their shape. *Nature Reviews Molecular Cell Biology*, 8(3):258–264, Feb 2007. doi: 10.1038/nrm2119.

P. Walter and D. Ron. The unfolded protein response: From stress pathway to homeostatic regulation. *Science*, 334(6059):1081–1086, Nov 2011. doi: 10.1126/science.1209038.

M. C. Watson, A. Morriss-Andrews, P. M. Welch, and F. L. H. Brown. Thermal fluctuations in shape, thickness, and molecular orientation in lipid bilayers. II. Finite surface tensions. *The Journal of Chemical Physics*, 139(8), Aug 2013. ISSN 0021-9606. doi: 10.1063/1.4818530. 084706.

L. M. Westrate, J. E. Lee, W. A. Prinz, and G. K. Voeltz. Form follows function: The importance of endoplasmic reticulum shape. *Annual Review of Biochemistry*, 84:791–811, Jun 2015. doi: 10.1146/annurev-biochem-072711-163501.

L. Xuemei, Z. Kezhong, and L. Zihai. Unfolded protein response in cancer: the

physician's perspective. *Journal of Hematology & Oncology*, 4, 2011. doi: 10.1186/1756-8722-4-8.

H. Yoshida, T. Matsui, A. Yamamoto, T. Okada, and K. Mori. XBP1 mRNA is induced by ATF6 and spliced by IRE1 in response to ER stress to produce a highly active transcription factor. *Cell*, 107(7):881–891, Dec 2001. doi: 10.1016/S0092-8674(01)00611-0.

Appendix A: Appendix

This appendix demonstrates the convergence test of replica exchange umbrella simulations and uncertaineity calculation of ΔE_{p} and ΔE_{γ} .

A.1 Convergence analysis

For each tension case, a convergence test was done in the following method; the longest simulation is taken as the ground truth or reference, T_{total} and the total simulation was divided into several segments, T_{i}, where i represents a segment of total simulation trajectory. The root mean square error of free energy profile of IRE1 dimer dissociation computed by i^{th} simulation compared to reference free energy profile of IRE1 dimer dissociation(T_{total}) is calculated by following equation:

$$RMSE_i = \sqrt{\sum_{j=5}^{71} \frac{F_t(j) - F_i(j)}{n}} \tag{A.1}$$

Where n represents the number of reaction coordinates in the free energy landscape. $F_{\mathrm{t}}(j)$ and $F_{\mathrm{i}}(j)$ represents the free energy of the total simulation and free energy of the segment i at reaction coordinate j in terms of kJ/mol-K respectively. Plot of $RMSE_{\mathrm{i}}$ against the independent segments of simulation shows that increasing the simulation time reduces the $RMSE_{\mathrm{i}}$ because of increased samplings. Fig. A.1 shows a plot of RMSE against different simulation timescales for bilayer tension 15 pN/nm. Panel A.1a shows free energy landscapes of three independent 1 μs simulations compared to the free energy profile of a total 3 μs simulation. Similarly, Fig A.2, A.3, and A.4 show the convergence of bilayer tension 5, 0, and -5 pN/nm, respectively.

Numerical parameters

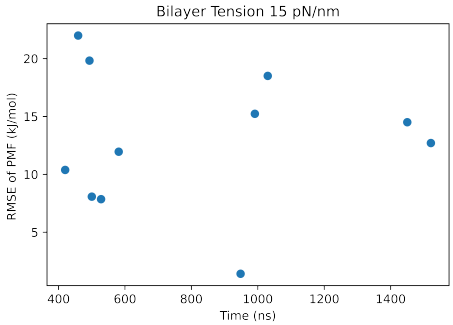

(a) RMSE values of free energy profiles of independent simulations with respect to total simulation.

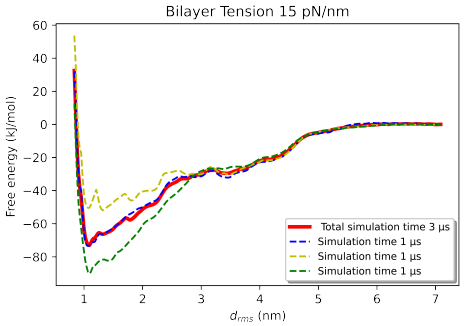

(b) Free energy profiles of three independent 1 μs simulations compared to reference 3 μs simulation.

Figure A.1: Convergence analysis of free energy landscape of IRE1 dimer dissociation at bilayer tension 15 pN/nm.

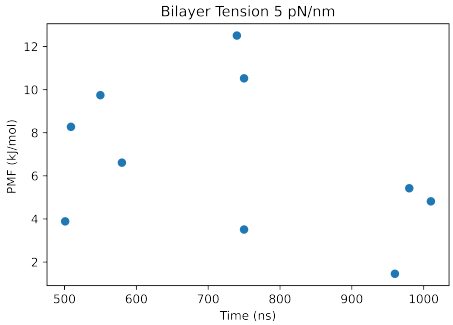

(a) RMSE values of free energy profiles of independent simulations with respect to total simulation.

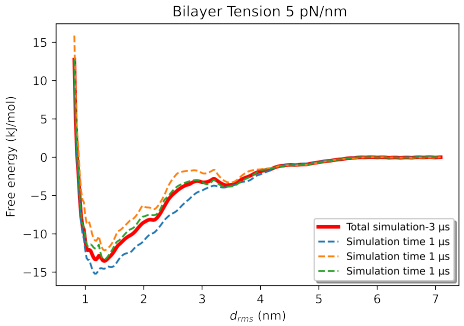

(b) Free energy profiles of three independent 1 μs simulations compared to reference 3 μs simulation.

Figure A.2: Convergence analysis of free energy landscape of IRE1 dimer dissociation at bilayer tension 5 pN/nm.

A.1.1 Estimation of thickness modulus

The thickness modulus of the lipid composition, K_t was estimated by following equation[Watson et al., 2013, Bitbol et al., 2012]

$$a_\gamma = a_{\gamma 0}(1 - \gamma/K_t) \tag{A.2}$$

where γ is the applied bilayer tension and a_γ and $a_{\gamma 0}$ is the unperturbed bilayer thickness at the bilayer tension γ and 0 respectively. To calculate the a_γ and $a_{\gamma 0}$, we have divided the entire 3 μs simulation trajectory into independent sections of 1 ns

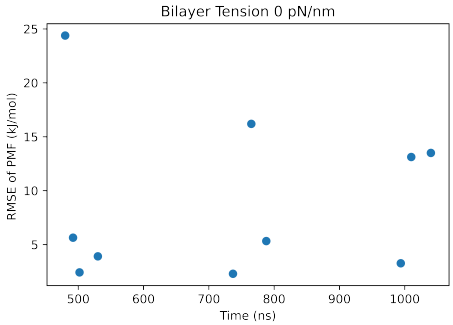

(a) RMSE values of free energy profiles of independent simulations with respect to total simulation.

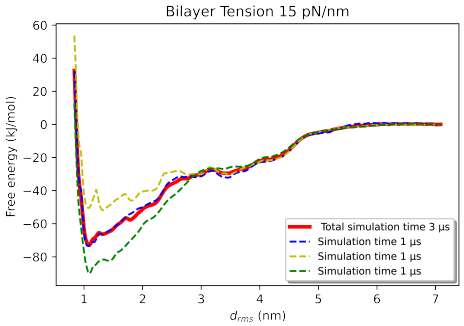

(b) Free energy profiles of three independent 1 μs simulations compared to reference 3 μs simulation.

Figure A.3: Convergence analysis of free energy landscape of IRE1 dimer dissociation at bilayer tension 0 pN/nm.

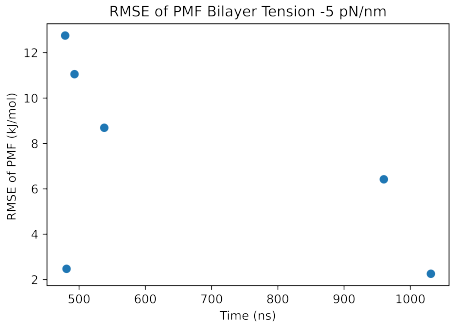

(a) RMSE values of free energy profiles of independent simulations with respect to total simulation.

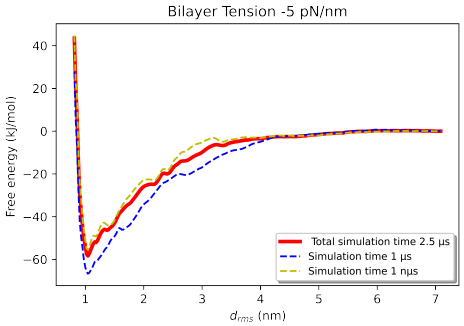

(b) Free energy profiles of two independent 1 μs simulations compared to reference 2.5 μs simulation.

Figure A.4: Convergence analysis of free energy landscape of IRE1 dimer dissociation at bilayer tension -5 pN/nm.

simulation and calculated the far field average of membrane thickness with the help of VMD plugin MEMB and python codes. By plotting the a_γ and $a_{\gamma 0}$ against the applied bilayer tension γ, we estimated the K_t to be 480 pN/nm.

A.1.2 Calculation of ΔE_p

For calculation of ΔE_p, following equation was used

$$\Delta E_\mathrm{p} = \frac{K_t}{2} \int \int \left[\left\{ \left(\frac{h(x,y) - a_{\gamma 0}}{a_{\gamma 0}} \right)^2 - \left(\frac{a - a_{\gamma 0}}{a_{\gamma 0}} \right)^2 \right\} \right] dx\, dy \qquad \text{(A.3)}$$

First, we have determined the unperturbed bilayer thickness at zero tension, $a_{\gamma 0}$. To calculate unperturbed, we have used membrane thickness plot of three independent 1 μs simulation trajectories of single IRE1$^{516\text{-}571}$ monomer into 50% DOPC-50%POPC lipid. The unperturbed thickness of tensed/compressed ER was also calculated by analyzing three independent 1 μs simulations totaling 3 μs simulations. For each 1 μs simulation trajectory, membrane thickness plots were produced via the MEMB plugin of VMD. a for each tension case was calculated by averaging bilayer thickness far from the position of IRE1$^{516\text{-}571}$ inclusion. The heat map of membrane thickness of 1 μs trajectory under bilayer tension 5 pN/nm is shown in Fig. A.5a. The unperturbed membrane thickness was calculated by averaging the thickness over the surface, excluding the area influenced by the inclusion of IRE1$^{516\text{-}571}$. The membrane area depressed by IRE1$^{516\text{-}571}$ is highlighted by a blue circle in Fig. A.5a. Next, membrane deformation, $u(x,y) = h(x,y) - a$ is shown in Fig. A.5b. For uncertainty calculation of ΔE_{p}, ΔE_{p} can be arranged as follows

$$\begin{aligned}
\Delta E_{\mathrm{p}} =& \frac{K_t}{2} \int \int \left[\left\{ \left(\frac{h(x,y) - a_{\gamma 0}}{a_{\gamma 0}} \right)^2 - \left(\frac{a - a_{\gamma 0}}{a_{\gamma 0}} \right)^2 \right\} \right] dx\, dy \\
&= \frac{K_t}{2} \int \int \left(\frac{h(x,y) - a_{\gamma 0}}{a_{\gamma 0}} \right)^2 dx\, dy - \frac{K_t}{2} \int \int \left(\frac{a - a_{\gamma 0}}{a_{\gamma 0}} \right)^2 dx\, dy \\
&= \Delta E_{\mathrm{p1}} - \Delta E_{\mathrm{p2}}
\end{aligned} \tag{A.4}$$

Then, the uncertainty of ΔE_{p} was estimated by following equation

$$\Delta \Delta D_p = \sqrt{\left(\frac{\partial \Delta E_{p1}}{\partial a_{\gamma 0}} \Delta a_{\gamma 0} \right)^2 + \left(\frac{\partial \Delta E_{p2}}{\partial a_{\gamma 0}} \Delta a_{\gamma 0} \right)^2} \tag{A.5}$$

where $\Delta a_{\gamma 0}$ was determined by calculating three independent 1μs trajectories of single IRE1$^{516\text{-}571}$ monomer in 50% DOPC-50%POPC lipid at bilayer tension zero. $\frac{\partial \Delta E_{p1-2}}{\partial a_{\gamma 0}}$

were determined as follows

$$\frac{\partial \Delta E_{p1}}{\partial a_{\gamma 0}} = \frac{K_t}{2} \int \int \left[\frac{-2h(x,y)}{{a_{\gamma 0}}^3} \{h(x,y) - a_{\gamma 0}\} \right] dx\, dy \tag{A.6}$$

$$\frac{\partial \Delta E_{p2}}{\partial a_{\gamma 0}} = \frac{K_t}{2} \int \int \left[\frac{-2a}{{a_{\gamma 0}}^3} \{a - a_{\gamma 0}\} \right] dx\, dy \tag{A.7}$$

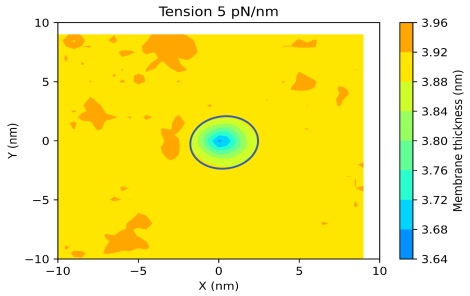

(a) Membrane thickness plot averaged over 1μs simulation of single IRE1$^{516\text{-}571}$ in 50%DOPC-50%POPC under application of bilayer tension 5 pN/nm. IRE1$^{516\text{-}571}$ locally depressed the membrane. A blue curve encloses the membrane depressed by IRE1$^{516\text{-}571}$. Unperturbed membrane thickness, a was calculated by averaging the membrane area excluding the area depressed by IRE1$^{516\text{-}571}$.

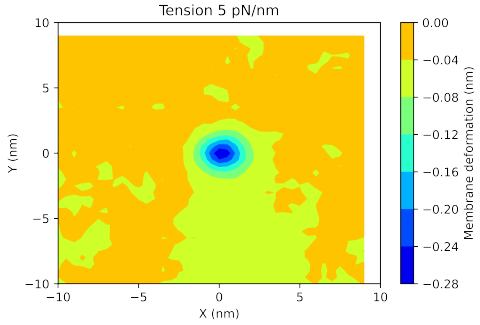

(b) Membrane deformation field of single IRE1$^{516\text{-}571}$ monomer in 50%DOPC-50%POPC averaged over 1 μs simulation at bilayer tension -5 pN/nm.

Figure A.5: Membrane thickness and membrane deformation field under application of 5 pN/nm. These membrane thickness and deformation was used to calculate k_{t} and ΔE_{p} by using equation A.2 and A.3 respectively.

A.1.3 Calculation of ΔE_γ

ΔE_γ is the amount of energy required to increase the lipid area surrounding the IRE1$^{516\text{-}571}$ to conserve the ER volume. ΔE_γ can be expressed in terms of membrane deformation $h(x,y) - a$ as follows

$$\Delta E_\gamma = \gamma \int \int \frac{h(x,y) - a}{a_{\gamma 0}}\, dx\, dy, \tag{A.8}$$

$a_{\gamma 0}$ and, a were calculated in similar procedure described in section A.1.2. The uncertainty of the ΔE_γ is determined as follows

$$\Delta\Delta E_\gamma = \left(\frac{\partial \Delta E_\gamma}{\partial a_{\gamma 0}} \Delta a_{\gamma 0} \right) \tag{A.9}$$

where $\frac{\partial \Delta E_\gamma}{\partial a_{\gamma 0}}$ is calculated as

$$\frac{\partial \Delta E_\gamma}{\partial a_{\gamma 0}} = - \int \int \frac{\gamma}{{a_{\gamma 0}}^2} \left[h(x,y) - a \right] \, dx \, dy \tag{A.10}$$